8 Beam induced electron multipacting, electron cloud and vacuum design

Vincent Baglin and Oleg B. Malyshev

8.1 BIEM and e-cloud

8.1.1 Introduction

Beam induced electron multipacting (BIEM) and electron cloud (e-cloud) are two coupled effects that can compromise the performance of modern high intensity machines with positively charged beams. E-cloud was first observed on the proton storage ring (PSR) at the Institute of Nuclear Physics (Novosibirsk, Russia) in 1965 [1,2,3]. A few months later the e-cloud related instability was observed on ZGS at Argonne National Laboratory [4] and on AGS at Brookhaven National Laboratory [5] in USA. In the following years, the e-cloud has been detected and investigated in a number of other machines [6,7]:

- on Bevatron at Lawrence Berkeley National Laboratory (1971) [8], on PSR at Los Alamos (1986) [9], on AGS booster [10] in 1998 and on RHIC [11] in 2001 at the Brookhaven National Laboratory, on PEP-II in 2000 at SLAC [12], on Main Injector at Fermi National Laboratory in 2005 [13], on SNS in 2006 at Oak Ridge National Laboratory [14] and on CesrTA in 2009 at Cornell University [15] in USA;
- on ISR in 1972 [16], on PS in 2000 [17] on SPS in 1999 [18] and on LHC in 2010 [19,20] at CERN (Switzerland);
- on KEK PF in 1988 [21] and on KEKB in 2000 and 2017 [22,23] in Japan;
- on DAΦNE at LNF/INFN in 2003 [24] in Italy;
- on PETRA-III at DESY in 2009 [25] in Germany;
- ISIS at RAL in 2008 [26] in UK.

The electron cloud problem has also been intensively studied for future machines such as CLIC [27], HL-LHC [28], ILC [29,30] and FCC [31,32].

Such a strong and long-term interest to e-cloud problem highlights its importance for the beam dynamics:

- e-cloud can drive very fast, often destructive, beam instabilities (both single and multi-bunch);
- The space charge of the e-cloud focuses the positively charged beam thus leading to the betatron tune shift and energy spread. This can negatively affect the beam dynamic aperture in storage rings and the beam-beam interaction in colliders.

The BIEM process can qualitatively be described as follows. The initial electrons which appear in the beam chamber due to synchrotron radiation induced photoelectrons or due to beam induced gas ionisation can be accelerated in the electric field of the passing bunches, acquire kinetic energies of up to several hundreds of eV and then collide with the beam pipe walls and produce secondary electrons. When the electromagnetic

field generated by the bunch train create the resonant conditions, the electron multipacting can be triggered in.

All these electrons create a negative space charge along the beam path and form an electron cloud (e-cloud), thus the beam bunches are circulating in modified conditions:

- interacting with a space charge may cause the beam emittance growth above a tolerable level;
- which in conjunction with the collisions between beam particles and e-cloud electrons may increase the beam particle loss rate.

Furthermore, electron multipacting cause the following negative impacts:

- The BIEM transfers energy from the beam to the vacuum chamber walls, thus this increases:
    - the beam energy loss, requiring more power for the RF cavities to compensate the loss;
    - the heat of vacuum chamber, the power of such additional heat loads on a cryogenic vacuum chamber could become critical for its cryogenic system.
- Electron stimulated desorption (ESD) due to multipacting electrons will increase the gas density which can in its turn increase:
    - the beam particle loss rate,
    - the rate of electron production due to residual gas ionization.

Figure 1 illustrates the electron cloud build-up in the LHC beam pipe. Synchrotron radiation emitted in the dipole magnets by the proton beams generates photoelectrons from the photon interaction with the vacuum chamber wall. Since these photoelectrons are in quasi-synchronism with the proton bunch, they can be accelerated by it towards the opposite vacuum chamber wall. In the LHC, taking into account the pipe diameter and the bunch population, the photoelectrons bombard the vacuum chamber wall at about ~ 200 eV. As a consequence, secondary electrons are created and emitted into the beam pipe. If these secondary electrons have not been absorbed by the vacuum chamber wall when the 2^{nd} bunch passes, they can be accelerated towards the wall. In this illustration, the low energy secondary electrons (1 and 5 eV) are in the vicinity of the bunch when it arrives 25 ns latter. Therefore, these secondary electrons receive a larger kick from the bunch, bombarding the vacuum chamber wall in the keV range. Secondary electrons are then produced and emitted into the beam pipe. When cumulated with the following bunches, this process, called BIEM, results in a multiplication of the electrons into the beam pipe.

In this example, the seed of electrons originates from the photoelectron production, which is the dominant process in LHC. However, the seed of electrons can also originates from beam gas ionization or particle loss at the vacuum chamber wall.

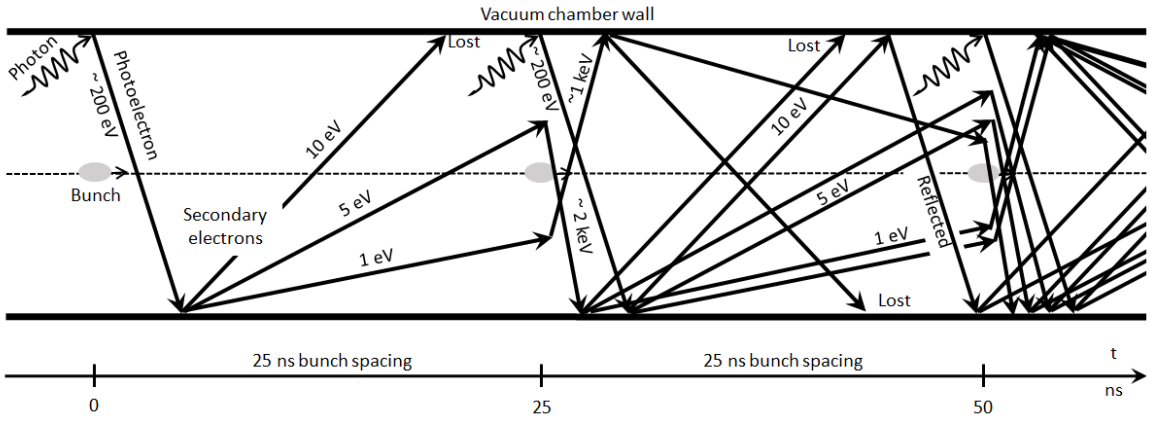

Figure 1: Illustration of BIEM and electron cloud build-up in the LHC beam pipe.

Note 1: In general, e-cloud could appear without BIEM, when the main sources of electrons are gas ionization and/or photoemission. From another side, BIEM would not necessary create the e-cloud with an electron density above a tolerable level. It is also worth mentioning that the RF cavities and waveguides may also suffer from electron multipacting, while e-cloud is not an issue there.

Note 2: Theoretically, BIEM could be triggered on in the very high intensity machines with negatively charged bunches [33]; the electron cloud effects for an electron-beam was studied both theoretically and experimentally in some machines [34,35,36].

Since the discovery of e-cloud and its impact on beam dynamics there was a significant effort in looking for various techniques of e-cloud mitigation. This activity was intensified in last 20-25 years with the design and operation of high intensity and low emittance colliders such as SSC, LHC, ILC, KEK-B, SuperKEKB, DAFNE, PEP-II, etc. These studies are covering a number of activities such as:

- Photon electron yield (PEY) and secondary electron yield (SEY) measurements of various materials after different treatments, coatings, conditioning, etc.;
- Photon reflectivity of these materials;
- BIEM and e-cloud modelling;
- BIEM and e-cloud studies in the machines;
- Developing various BIEM and e-cloud mitigation techniques.

8.1.2 E-cloud models

Approximated equations, based on a stationary electron model, can be derived to evaluate the possible existence or not of BIEM and electron cloud in a machine [37].

A first condition to allow wall-to-wall electron multipacting is that the electrons cross the beam pipe of radius r_p, between the successive bunch passages timely spaced by t_{bb}. Assuming a bunch of uniform transverse density, the minimum electric field required to provide enough speed to the electrons can be computed. This translates in a minimum bunch population, N_b, given by:

$$N_b \geq \frac{{r_p}^2}{r_e c\, t_{bb}} \qquad (8.1)$$

where $r_e = 2.8\times10^{-15}$ m is the classical electron radius, and c the speed of light .

A second condition for electron multipacting is that the energy of the electron bombarding the wall shall be large enough to allow the production of secondary electrons. For this reason, the energy gain by the electron from the passing beam bunch shall be computed. In the simple kick approximation, the energy gain to the electron, $\Delta W(r)$, received by the kick from the bunch field as a function of the radial position r, is given by:

$$\Delta W\left(r\right) = 2mc^2 {r_e}^2 \left(\frac{N_b}{r}\right)^2, \qquad (8.2)$$

where m = 511 keV/c^2 is the electron mass.

In the previous calculation, the transverse bunch density is assumed uniform. Therefore, the electric field outside the bunch falls-off proportionally to $1/r$. In a real machine, the transverse r.m.s. beam size of a beam σ is described by the Gaussian distribution modifying the electric field within the beam pipe. However, at a distance larger than 2σ, the difference between the simple kick approximation and the real electric field is negligible. Thus, the simple kick approximation is valid for electrons, which are located at the distance of a few beam radius away from the bunch. In particular, the previous equation is valid near the vacuum chamber wall.

Figure 2 (left), shows the minimum bunch population required to allow a wall to wall multipacting as a function of bunch spacing for several vacuum chamber radii (see Eq. (8.2)). It is seen that a bunch population in the range of 10^{11} particle per bunch will generally trigger multipacting for almost any bunch spacing and medium size (ID* ~80 mm) vacuum chambers. It must be stressed that the bunch population is computed for a multipacting to occur between each bunches.

Figure 2 (right), shows the energy gain received during the passage of the bunch by a stationary electron at several location in the vacuum chambers (Eq. (8.2)). For a bunch population in the range of 10^{11} particle per bunch, the energy gain received by the electron is 50 eV for electrons located at 40 mm from the bunch and increase to 800 eV for electrons located at 10 mm from the bunch. For positions closer to the beam (*i.e.* < 10 mm), the movement of the electron during the passage of the beam shall be taken into account. A more accurate evaluation of the energy gain can be then obtained by integrating the equation of motion.

* ID is an inner diameter of a beam pipe

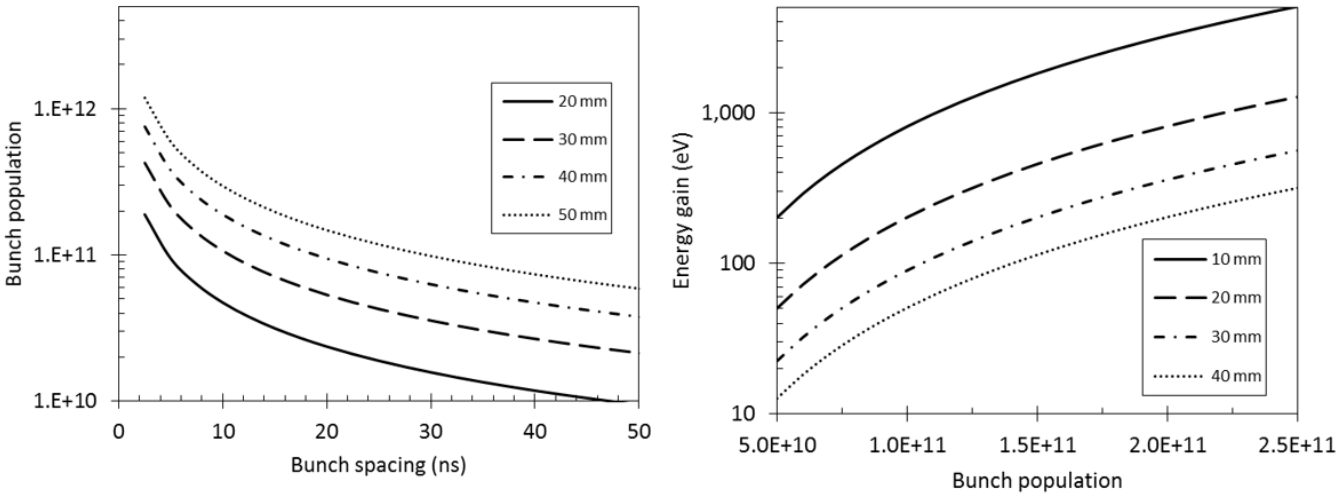

Figure 2: Left, minimum bunch population for a wall-to-wall multipacting as a function of bunch spacing for several vacuum chambers radii; right, energy gain received by the electron from the bunch kick as a function of the bunch population for several electron positions in the vacuum chamber.

The average energy gain in kinetic energy of an electron cloud stationary in time and uniformly distributed is given by:

$$\langle \Delta W \rangle = 6mc^2 {r_e}^2 \left(\frac{N_b}{r_p} \right)^2 , \qquad (8.3)$$

This handy formula can be used to evaluate the ESD yields (which are a function of the energy) of a vacuum chamber subjected to BIEM or to evaluate the deposited heat load if the electron flux to the wall is known.

Figure 3 shows the average kinetic energy gain of a stationary and uniformly distributed electron cloud for several vacuum chamber radii. For a bunch population of 10^{11} particle per bunch, the average kinetic energy varies from 30 to 200 eV when decreasing the vacuum chamber inner diameter from 100 to 40 mm.

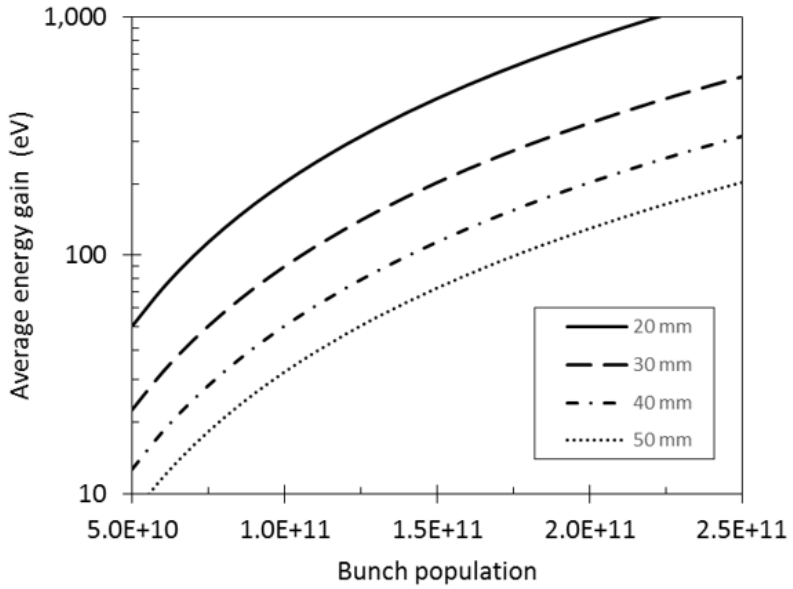

Figure 3: Average kinetic energy gain of a stationary and uniformly distributed electron cloud for several vacuum chamber radii.

When dealing with magnetic fields, complex vacuum chamber shapes or specific beam structures, a better evaluation of the BIEM and electron cloud parameters can only be achieved by simulation codes *e.g.* PyECLOUD, CLOUDLAND, CSEC, POSINST, Factor2, etc. [38,39]. Figure 4 shows the simulated heat load and electron current at the vacuum chamber wall as a function of the SEY in a beam screen dipole of the LHC. This simulation is computed with PyECLOUD.

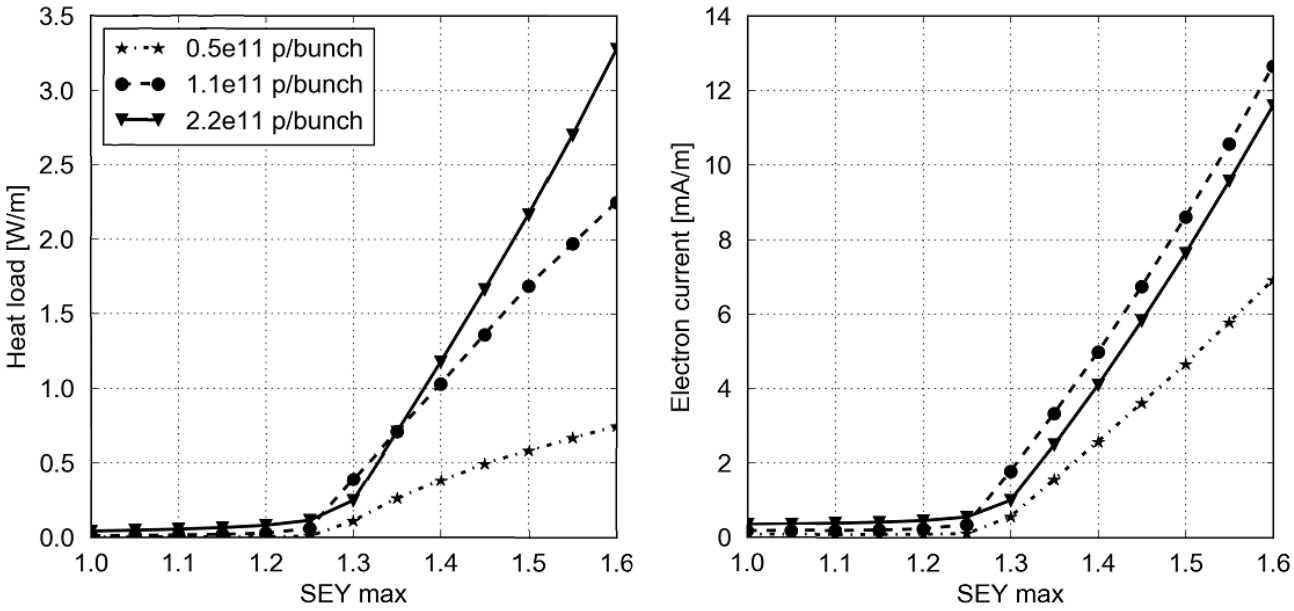

Figure 4: Simulated heat load and electron current as a function of the SEY in a beam screen dipole of the LHC when operated at 7 TeV with different bunch population. Data are obtained from PyECLOUD simulation code in Ref [40].

In absence of magnetic field, the electron cloud interacts only with the circulating bunches and the vacuum chamber wall. The motion of the electrons is not guided, and the cloud occupies the full cross section. As shown in Figure 5, in the presence of a positively charged bunch, the electrons are repelled towards the vacuum chamber walls (left side). When the kicked energy is large enough, some secondary electrons can be produced and drift inside the vacuum tube ready to be kicked again towards the wall by the following bunch (right side) [41].

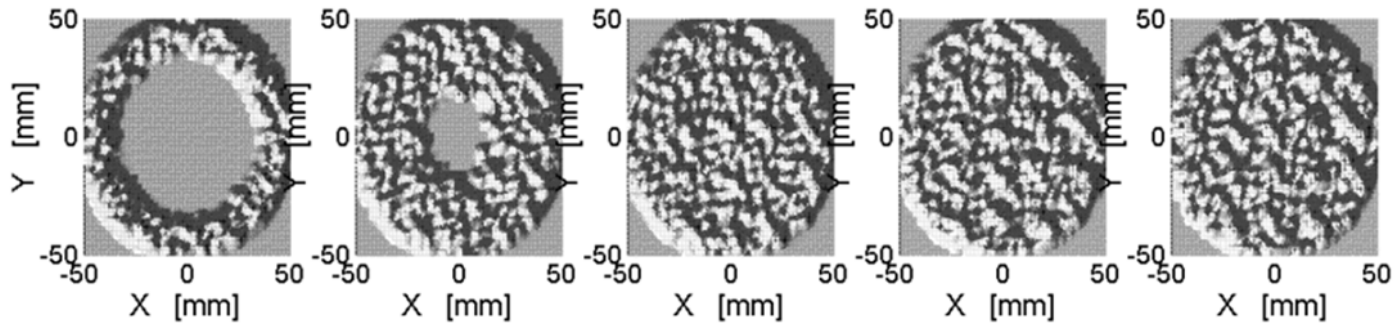

Figure 5: Electron cloud cross section distribution in absence of magnetic field during the passage of the bunch, left, and after the passage of the bunch, right. Slide 11 in Ref [41].

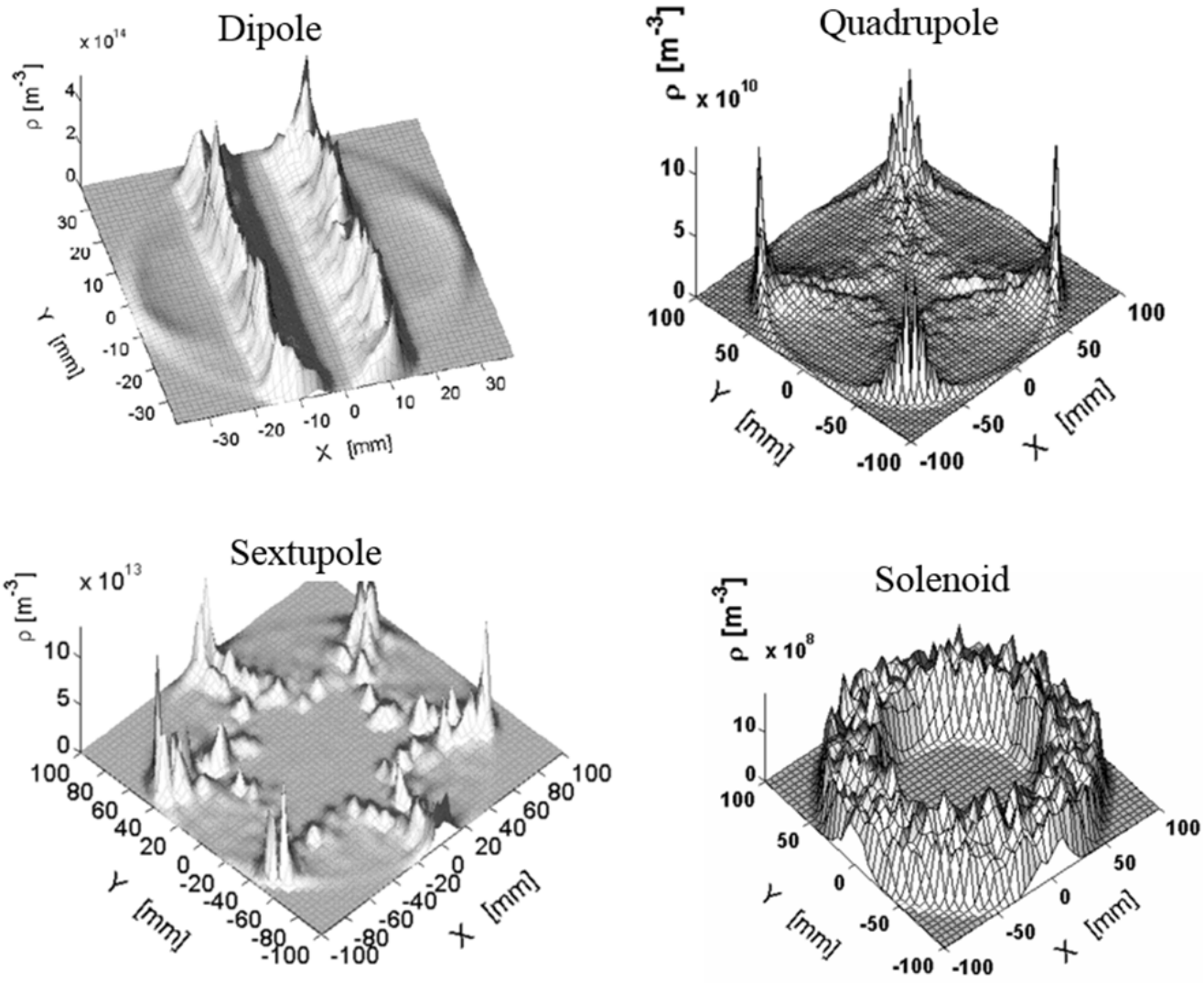

Figure 6: Effect on the magnetic field configuration on the electron cloud transverse distribution. Adaptation of Fig. 10 in Ref. [42] and Fig 25 and 26 in Ref. [43].

In the presence of a magnetic field, the electron motion is guided by the magnetic field lines. Figure 6 shows the transverse distribution of the electron cloud density for dipole, quadrupole, sextupole and solenoid fields. In the case of a dipole field, the electrons motion forms two stripes. The position of the stripes is a function of the bunch density and dipole field. The electron cloud interacts only with the upper part and lower part of the vacuum chamber. For the cases of the quadrupolar and sextupolar fields, the electrons motion follows the field lines and interacts with the vacuum chamber wall at the poles position. Applying a solenoid field maintains the electron cloud close to the vacuum chamber walls along its perimeter. In this case, the kick received from the bunch is minimised and, in the occurrence the electrons receive enough energy to produce secondary electrons, the energy of the secondary electrons being very low, they are maintained in the close vicinity of the wall chamber [42,43].

Input parameters for the BIEM and electron cloud phenomena depend on the shape of the vacuum chamber and its surface properties. BIEM in the vacuum chamber causes the electron stimulated gas desorption and may require modification of the vacuum system to deal with it. These input characteristics for BIEM and e-cloud modelling will be discussed the following sections of this Chapter.

8.2 Mitigation techniques and their impact on vacuum design

There are three main sources of electrons for BIEM and e-cloud in vacuum chamber [44]:

1. Electrons that appear due to *residual gas ionization* by the beam particles;
2. *Photo-electrons* that were emitted from vacuum chamber walls due to synchrotron radiation, see Chapter 3;
3. *Secondary electrons* emitted due to electrons multipacting, see Section 8.3 below.

Apart these three main sources there could be a few additional that may contribute into the process:

4. Electrons that appear due to *residual gas ionization*
    - by multipacting electrons and
    - by SR;
5. Bremsstrahlung photon, that appear due to beam-gas collisions, can contribe to
    - gas ionization and
    - photoelectron emission;
6. Beam particles hitting vacuum chamber, collimators and tapers may cause
    - secondary electron emission,
    - Bremsstrahlung radiation and, therefore, photo-electron production.

To lower the BIEM intensity and the e-cloud density, these sources of electrons must be minimised or even suppressed. Thus, the production of electrons due to residual gas ionization can be mitigated by specifying the maximum gas density, which requires using vacuum chambers with low photon and electron stimulated desorption (PSD and ESD) yields and providing sufficient (preferably distributed) pumping speed. Production of photo-electron emission due to synchrotron radiation is proportional to a photon flux, so it can be reduced by reducing the photon flux irradiating *the beam vacuum chamber walls* using photon traps, photon absorbers, antechambers, etc. Production of both photo-electrons and secondary electrons could be reduced by aiming reducing their production rates: photo-electron yield (PEY) and secondary electron yield (SEY) defined as a number of photo-electrons or secondary electrons, respectively, per impact of photon or electron.

A large number of BIEM and e-cloud mitigation methods have been developed over recent years. These mitigation methods can be divided into two groups: passive (i.e. they require no controllers or power sources after installation or implementation) and active (requiring controllers, power sources, feedback electronics, etc.).

Various solution can be applied, the choice is dictated by a few criteria. First of all, a chosen solution must solve the e-cloud and/or BIEM problem. Among working solutions, the most preferable one should be simple, cost effective and very reliable in long terms. Ideally, the preferred solution should works for a duration of machine lifetime, it does not take space, it does not require controllers and feedthrough.

8.2.1 Passive methods

Passive methods are implemented as an integrated part of the vacuum chamber, they don't require controllers, power sources, feedthroughs, feedback electronics, etc., once implemented they should work for a full lifetime of machine without maintenance. If a passive method works (*i.e.* reduces BIEM and e-cloud to below a tolerable level) for a whole machine or its sections then it is a preferable solution. Thus, a significant effort was made to find and develop a number of passive mitigation solutions [45,46,47,48].

(1) The PEY and SEY are related to surface material and chemical state, thus the significant interest was attracted to the materials and surface coating with material which have a low intrinsic SEY:

- Material have different PEY/SEY, for example, Cu has lower SEY than Al, see Figure 15 and Figure 16:
  - The PEY/SEY of as-received materials with a natural oxide layer [49,50,51,52];
  - The PEY/SEY of specially treated surface, for example etched and controlled oxidation, nitration or carbonation [53,54,55,56,57,58];
  - The PEY/SEY of pure materials after scrubbing with SR, electrons or ions in vacuum [14-16,21];
  - Effect of temperature and cryosorbed gases [59,60].
  - Pro: a simple choice from a short list of materials and low cost treatments;
  - Contra: a limited choice of materials compatible with vacuum chamber specifications.

- Coating any material with low PEY/SEY materials, see Figure 17:
  - TiN coating is a well-known technique with low PEY/SEY coating used in various application [61,62,63,64,65] ;
  - NEG coating [66] provides similar low PEY/SEY [61,67,68] combined with distributed pumping, *i.e.* a very good combined solution to suppress all three sources of electrons, thus, when a bake-out is acceptable, NEG coating is a preferred solution as an ideal for vacuum design due to low gas desorption and distributed pumping (see Chapter 5);
  - Amorphous carbon (a-C) coating [55,69,70]) lead to significant reduction of SEY ($\delta_{max}<1$) and suppression of electron multipacting;
  - Other low SEY coatings such as Cr, CrN, TiCr [71].

- Pro: it does not affect a choice of vacuum chamber materials, low SEY coating can be done on any vacuum chamber material;
- Contra: it requires using a vacuum based deposition technology, therefore increases the cost of the vacuum chamber.

(2) Surface geometry may help reducing the net SEY:

– Modifying a surface geometry by machining different shape grooves [45,72,73], see Figure 7, Figure 11 and Figure 18. Although the intrinsic SEY remains the same as for flat surface, the reduction of net SEY happens due to multiple interactions of electrons with grooves walls, thus higher probability of electron energy loss and electron absorption. The net SEY reduces with an increase of a ratio of height *h* to distance between grooves (*a* and *b* in Figure 7) and with decrease of rib width.

- Pro: it works;
- Contra: it required precise machining, thus may increase the cost considerably.

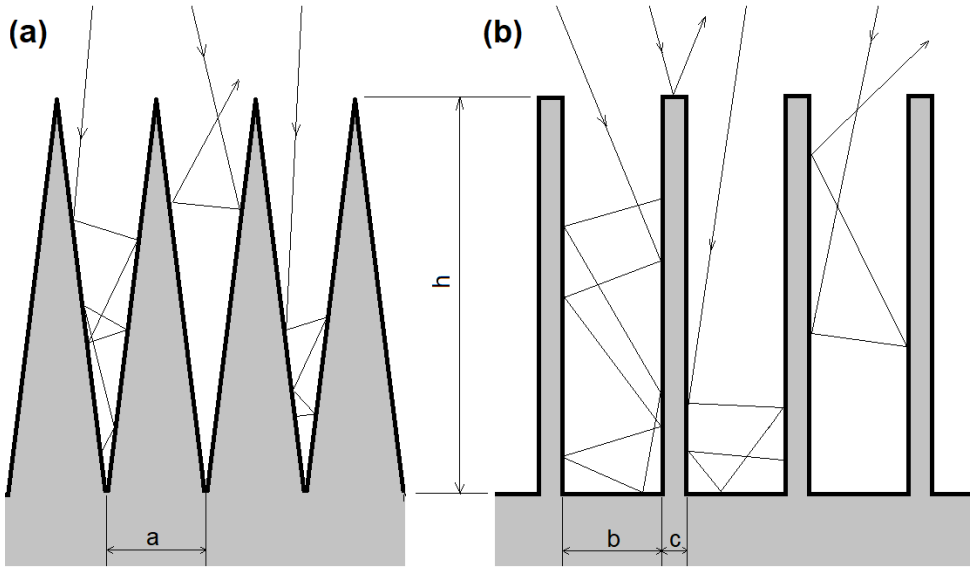

Figure 7. Two types of grooves for reducing the net SEY: (a) sawtooth-shaped grooves (*h* is a height and *a* is a distance between grooves); (b) rib-shaped grooves (*h* is a height, *b* is a distance between the ribs and *c* is a rib width).

– Coating with low SEY microstructure (ex.: copper black, gold black; columnar NEG) [68,74,75,76]:

  - Materials that grow in a form of columns, pyramids, nanotubes, flakes, could be very efficient in reducing PEY and SEY.

- Pro: it works;
- Contra: the created features could be fragile; cleaning with solvents could be difficult; a possibility of increasing thermal outgassing, PSD, ESD and ISD has to be investigated; there is a risk of particulate generation.

– Surface micro-engineering by ion etching, chemical etching, etc. [74], see Figure 8:
  - An technology that allows to rough the surface and reduce PEY and SEY.
  - Pro: it works;
  - Contra: the created features could be fragile; cleaning with solvents could be difficult; after this wet technology the surface is saturated with hydrogen thermal outgassing, PSD, ESD and ISD could increase; there is a risk of particulate generation.

–

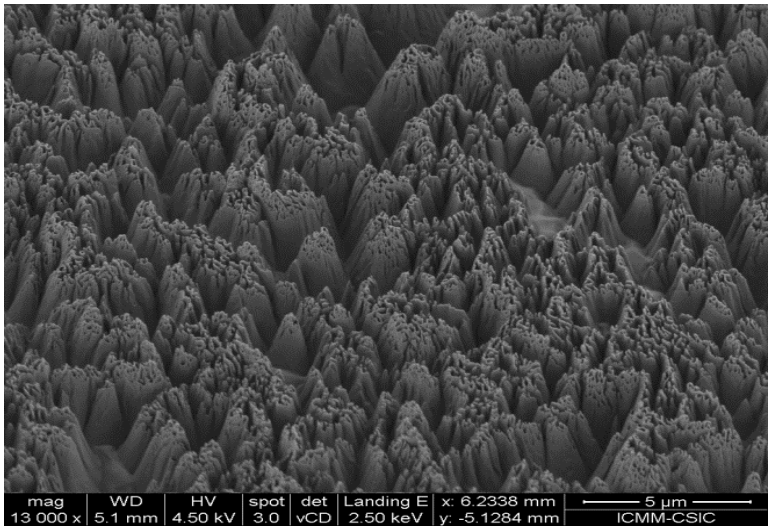

Figure 8. Ag plating, ion etched with Mo Mask (Fig. 3 in Ref. [74]).

– Laser ablation surface engineering [77,78,79,80], see Figure 19:
  - The most recently invented technology for reducing PEY and SEY, allowing to obtain low SEY with (δ_{max}<1) for as-received metal surfaces modified by a nanosecond pulsed laser. Bakeout or bombardment with electrons led to even lower value of δ_{max}<1 [81,82].
  - Pro: In comparison with other technologies used for surface engineering, the laser treatment has a few advantages such as simple equipment, the treatment does not require vacuum condition and it can be done in air under atmospheric pressure, reduces PSD, ESD and ISD.
  - Contra: it requires particulate control.

Note: all surface engineering technologies could increase the surface resistance, which, in turn, could potentially impact on the beam impedance.

(3) Vacuum chamber shape may help in e-cloud suppression:

– Using antechamber and shadowing critical components from SR is a very efficient mean to reduce the number of photoelectrons in beam chamber, the photoelectrons emitted in antechamber don't play a role in BIEM and e-cloud [83,84,85,73]:

- In comparison to photoelectrons emitted from the beam chamber walls, the photoelectrons produced in an antechamber are exposed to a much weaker beam electric field, they have a strongly reduced probability to enter the beam chamber through a narrow gap between the chamber and antechamber to participate in BIEM and e-cloud.
- SR absorbers in antechamber could have a special design to minimise the PEY, for example, absorbing photons at normal incident, photoelectron traps similar to a Faraday cup, using low PEY materials, etc.

- Pro: it takes away one of the main sources of electrons in the beam chamber and it allows to efficiently use the benefits of an antechamber when it is already considered in a vacuum chamber design (e.g.: for SR beamline, for higher vacuum conductance or for distributed pumping);
- Contra: a more complicate design and more expensive vacuum chamber than a simple (e.g.: round or elliptic) beam chamber.

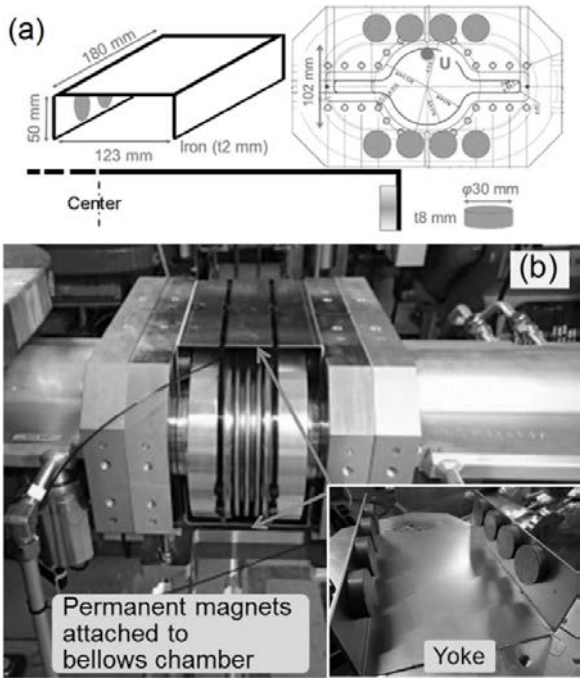

Figure 9: (a) schematics and (b) a photo of yokes with permanent magnets attached to the bellow chambers at SuperKEKB low energy ring (Fig. 12 and 11(b) in Ref. [86], respectively).

(4) Use of permanent magnet field for trapping electrons [48,86]:

- Permanent magnets are applied to suppress e-cloud at KEK-B, see Figure 9.

- Pro: it works, it is quite simple and low cost, it doesn't not require power controllers and cables, it can be installed at any stage of machine lifetime, it does not affect vacuum system as it is outside of vacuum chamber.

- Contra: it can only mitigate electron clouds in magnetic field-free areas, it may affect operations of BPMs, vacuum gauges and other sensitive equipment. Maximum bakeout temperature of these permanent magnets should be checked, it could be below the vacuum temperature bakeout temperature of 250-300 °C, in the latter case these magnets should be removed before and re-installed after each vacuum chamber bakeout.

(5) Various combinations of all the above can be applied as well [48,73], see Figure 10 and Figure 11:

a. Antechamber combined with grooves in the beam chamber;
b. Antechamber combined with TiN coating;
c. NEG coating on rough surface;
d. Any other possible combinations.

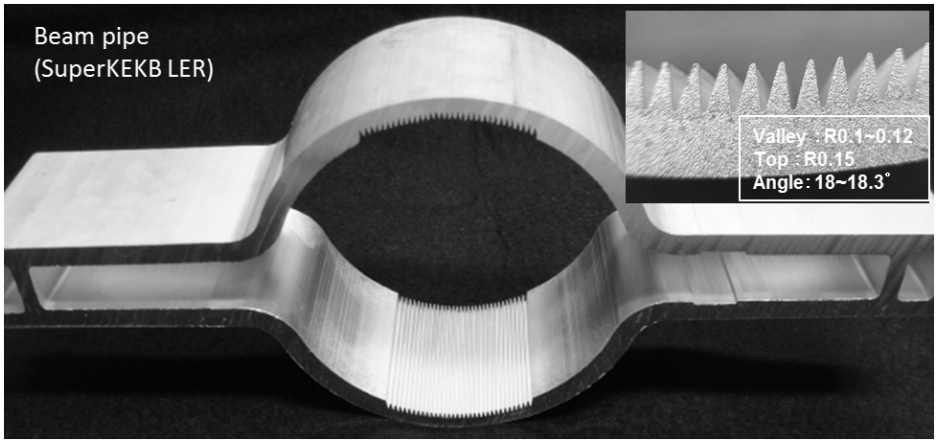

Figure 10. KEK vacuum chamber with grooves and an antechamber (Fig. 6 in Ref. [87]).

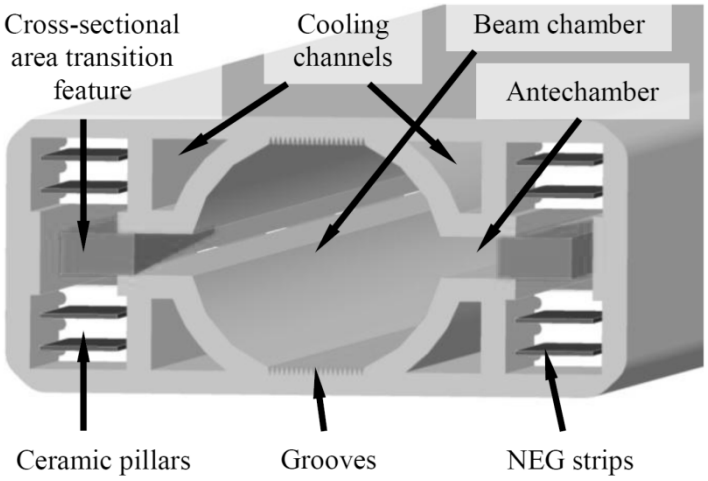

Figure 11. A layout of wiggler vacuum chamber in the ILC positron damping ring (Fig. 3 in Ref. [73]).

8.2.2 Active methods

Active methods are used in many machines, they could be used as a single solution or in combination with others, the examples of such methods, with their pro and contra are shown below.

(1) As shown in Figure 12, a weak solenoid field (~50 Gauss) can be applied along the drift chambers [88,89]. Magnetic field traps photo- and secondary electrons near the surface and away from the beam path, thereby reducing the BIEM and electron cloud as shown by the reduction of the pressure increase. Usually it is used in combination with TiN or NEG coating of such vacuum chambers.

- Pro: a coil can be added after the beginning of the machine operation to solve unexpected issues. It is can be easily implemented only on simple straight sections.
- Contra: requires winding the coils, cables, controllers and power supplies. Such solution might be not compatible with a bakeout system. It can be used in magnetic field-free regions only.

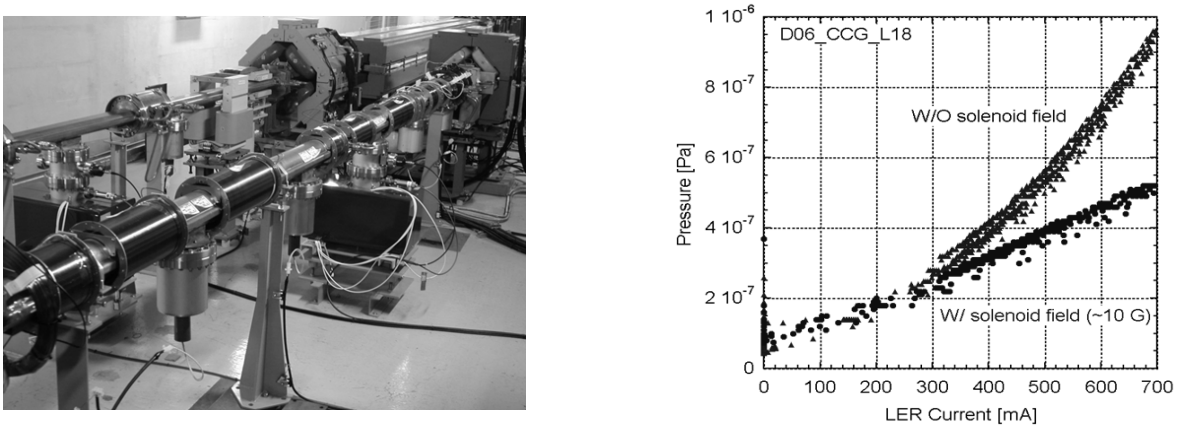

Figure 12: Left, KEKB low energy ring solenoids. Right, observation of pressure rise with and without solenoid field as a function of the positron beam current. The non-linear behaviour, signature of electron multipacting, is supressed when a solenoid field is applied. Picture Courtesy of Y. Suetsugu, KEK. Fig. 7 in Ref [89].

(2) Clearing electrodes (biased up to +/-1000 V) in wigglers and dipoles are not allowing electrons to multipact [47,90,91,92,93,94]. As shown in Figure 13, the clearing electrodes in the DAΦNE dipole chambers strongly reduces the horizontal instability even at large beam current.

- Pro: it works. It can be installed inside dipole, quadrupole and wigglers
- Contra: requires designing and manufacturing of these electrodes, redesigning and adopting a vacuum chamber to accommodate these electrodes, their holder and electric feedthroughs. Electrodes and insulating materials may dramatically increase the gas density in a vacuum chamber due to thermal, photon, electron and ion induced gas desorption. Choice of material for electrodes and insulating layer as well as in-vacua design must be UHV compatible, *i.e.* requires additional vacuum studies and testing. Feedthroughs increase the chance of vacuum leaks to air. It requires, cables, controllers/power supplies which significantly increase the cost for large machines.

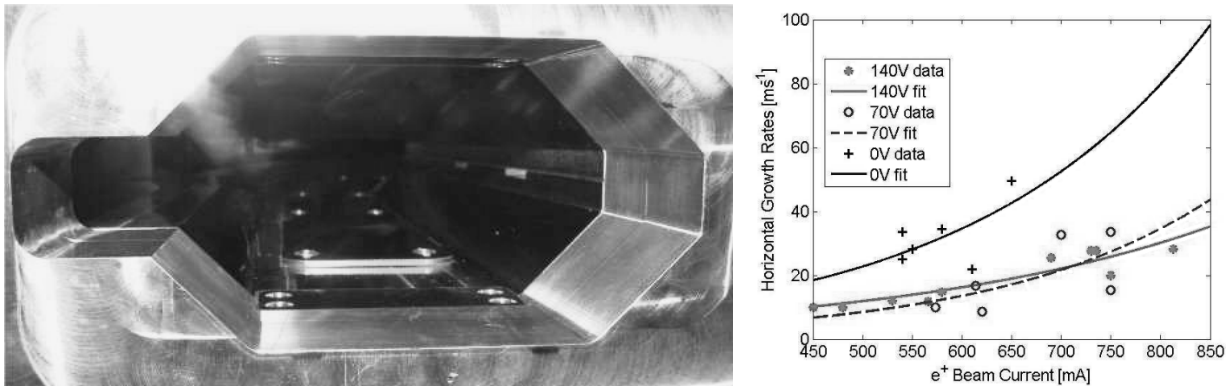

Figure 13. Left: clearing electrode in a DAΦNE dipole vacuum chamber; right: electron intensity grow rate (Figs. 5 and 14 in Ref [90], respectively).

(3) Optimising the beam train parameters to avoid high intensity resonant conditions by varying a beam charge and a beam spacing, introducing satellite beams, etc. [95,96].

- Pro: it also works. It requires no change in vacuum design, no additional cables, controllers and power supplies in the machine tunnel.
- Contra: it reduces the flexibility in machine operation. In high-energy particle colliders, it may results to more collisions per crossing thereby limiting the particle detectors efficiency.

8.2.3 Which techniques suits the best

It is important to mention that all the active and passive methods are working well and can be employed on its own or in various combinations with each other.

In general, different techniques could be the most efficient for different components and different sections of the machine. Thus, a machine design team should balance effort, efficiency, impact on various machines systems, costs, etc., and choose the techniques, which will suit the best for whole machine, for a sector or a particular component.

- First of all, the chosen BIEM and e-cloud mitigation technique must be explicitly fitted for the purpose.
- A simple solution is preferable as it is usually more robust.
- The cost of mitigation could vary for different techniques, thus an increase in the cost of vacuum chamber should be taken into consideration during the design phase.
- The mitigation technique should be vacuum compatible, and vice versa, a solution for beam vacuum chamber should be compatible with a BIEM and e-cloud mitigation technique.
- The mitigation techniques employed inside beam vacuum chambers (surface roughening, coatings, asymmetric vacuum chamber shape (e.g. due to an antechamber), clearing electrodes, etc.) may affect the longitudinal and/or transversal beam impedance. An implementation of such mitigation techniques would be recommended then an impact on the beam impedance is below a tolerable level.

– Therefore, a mitigation solution should meet all the requirements for BIEM and e-cloud mitigation, beam impedance, particulate generation, vacuum specification and machine risk analysis.

It must be noted here, that an implementation of mitigation techniques in a design phase is much easier, while solving the BIEM and e-cloud problem on an already existing and operating machine has a shorter list of possible solutions.

8.3 Secondary electron emission (laboratory studies)

8.3.1 SEY measurement method

When a primary electron interacts with matter, it causes the emission of secondary electrons. Primary electrons penetrate into the solid along 1-10 nm and produce secondary electrons. Those electrons can be scattered or diffused into the solid and might be consequently emitted into the vacuum. The total SEY (or δ) is defined as a total number of electrons emitted from the surface per incident electron:

$$\delta = \frac{I_S}{I_P}; \tag{8.4}$$

where I_S is the secondary electron current (including both elastic and inelastic processes) and I_P is the primary electron current.

A typical layout of secondary yield measurements is shown in Figure 14. During the SEY measurements, the sample is bombarded by electron with energy in range from 10 eV to 3 keV (depending on the operation range of connected electron gun). The sample can be biased between 0 and -100 V to repel secondary electrons toward the Faraday cap. The SEY measured with no bias are higher than with no bias. The SEY increases with a bias and reaches its saturation at certain bias value, which depends on the gap between the sample and a Faraday cap. In the experiments reported below the bias was always applies at the saturation value. Two currents can be measured simultaneously in the experiment: a sample drain current, I_D, and a current at the Faraday cap, I_F. The total SEY can be calculated as:

$$\delta = \frac{I_S}{I_P} = \frac{I_F}{I_F + I_D}. \tag{8.5}$$

An alternative method used to measure the SEY consists in doing the measurement in two steps. In a first step, the sample is biased negatively to repel the secondary electrons and the sample drain current, I_D, is measured. In a second step, the sample is replaced by a Faraday cup from which the primary electron beam current, I_P can be measured. The amount of secondary electrons is derived from the subtraction of the primary electrons current minus the sample drain current. In this case, the SEY is given by the following equation:

$$\delta = \frac{I_S}{I_P} = \frac{I_F - I_D}{I_F} = 1 - \frac{I_D}{I_F}. \tag{8.6}$$

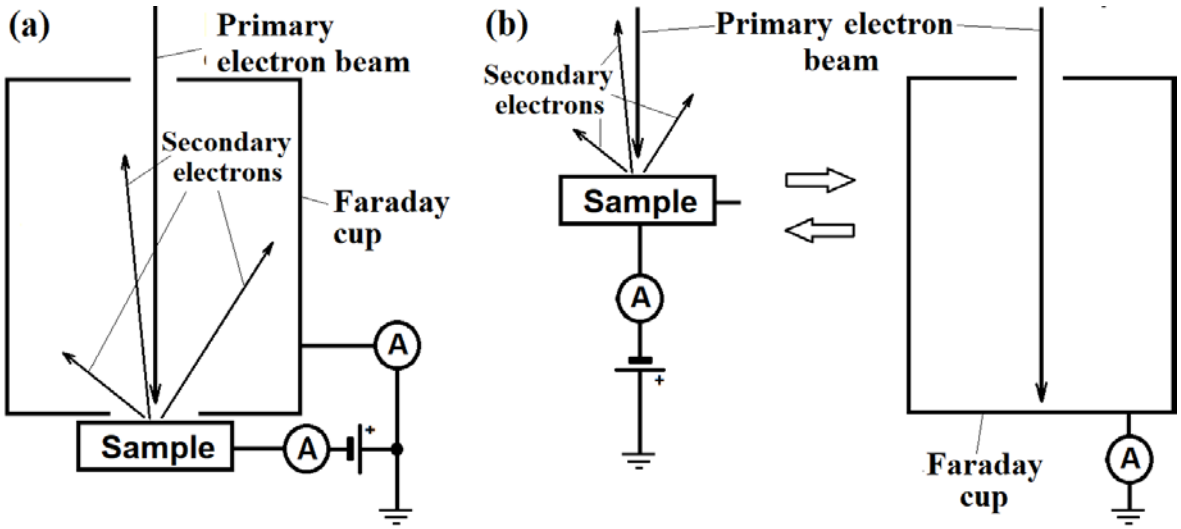

Figure 14. Typical layout of secondary yield measurements (a) simultaneous measurements of currents from a sample and a Faraday cup with a passing through primary electron beam, (b) two-step measurements of currents from a sample only and a close Faraday cup only.

In this section we summarise the main tendencies in SEY in various conditions.

8.3.2 SEY as a function of the incident electron energy

Figure 15 shows SEY curves of typical materials used for the construction of accelerator vacuum systems as a function of the incident electron energy. The values are given for 'as-received' unbaked material, *i.e.* without any specific treatment to reduce the yield [97]. The curves have a 'bell' shape with a maximum in the range 200-300 eV. The maximum of the SEY, δ_{max}, ranges from δ_{max} = 1.5 for TiN coated sample to δ_{max} = 3.5 for aluminium. Typical values for titanium, copper and stainless steel are around δ_{max} ~ 2. Any electrons bombarding a surface with a primary energy up to 2 keV will subsequently produce secondary electrons increasing the total amount of electron in the accelerator.

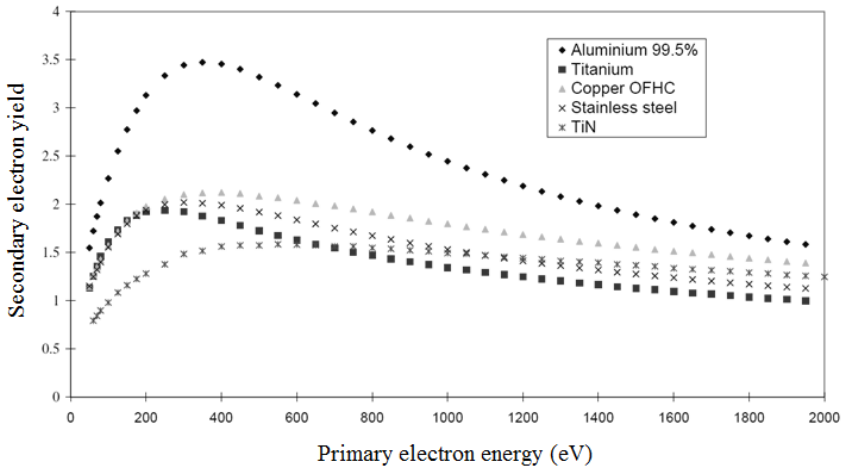

Figure 15: Secondary Electron Yield (SEY) curves of some technological materials used for the construction of accelerators. Fig 3 in Ref. [97].

8.3.3 Effect of surface treatment by bakeout, photon, electron and ion bombardments

As mentioned previously, several techniques are used to lower the SEY of technical surfaces. This is illustrated in Figure 16 (left side), where, for instance, the maximum SEY of copper surface reduces by baked at 300 ºC to $\delta_{max} \approx 1.7$. Cleaned copper surface, *i.e.* bombarded with Ar ions in a way to sputter the native oxide, hydrocarbon and contaminants layer, has a maximum SEY of $\delta_{max} \approx 1.4$ at a primary kinetic energy of ~650 eV [97]. Electron bombardment can also reduce the secondary electron yield of technological surfaces. This effect is often used in various equipment, *e.g.* radio-frequency cavities or accelerators, to mitigate the electron multipacting. Figure 16 (right side) shows the evolution of δ_{max} of an as-received Cu surface as a function of the electron dose. After bombardment with electron of kinetic energy above 50 eV, δ_{max} can be reduced to ~1.1. However, for lower kinetic energy and the same electron dose the conditioning is less efficient and the value of δ_{max} reaches ~1.35. The origin of this reduction phenomenon (called "scrubbing" or "conditioning" in accelerator scientist's jargon) is ascribed to removing oxides (by ESD) and the graphitization of the surface [54,68].

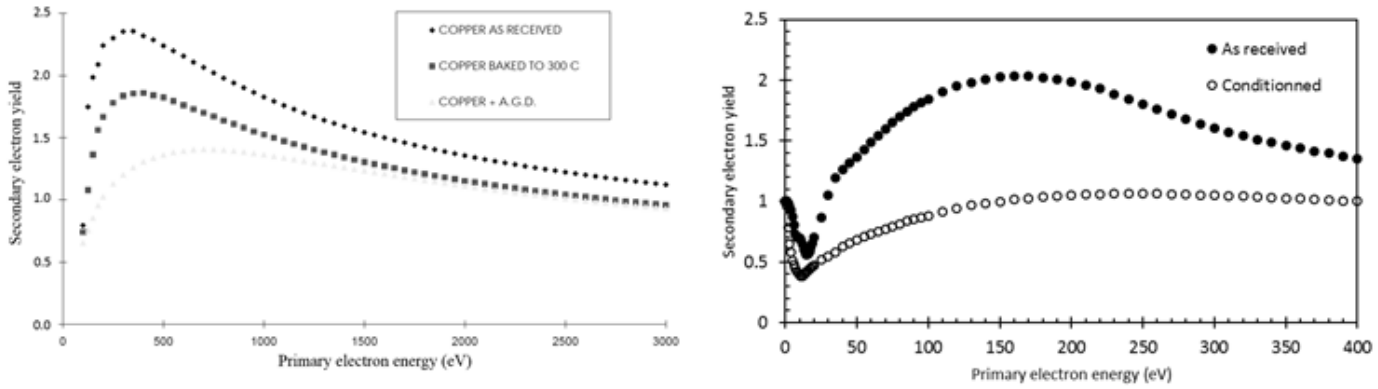

Figure 16: Secondary electron yield curves of Cu as a function of surface treatment: bakeout, Ar glow discharge (left), electron bombardment (right). Fig. 2 in Ref [97] and re-arranged data of Fig.2 in Ref [54].

8.3.4 Effect of surface material

Even cleaned following the UHV standards, the technological surfaces are covered by a surface layer consisting of oxides and physisorbed /chemisorbed gases, which modify the secondary electron emission of the pure material. An ion bombardment can sputter the contaminants removing then from the surface. As already shown in Figure 16, Cu has $\delta_{max} \approx 1.4$ when sputter cleaned under ion bombardment. Table 1 shows the maximum secondary electron yield, δ_{max}, and the corresponding impinging energy, E_{max}, of some common pure materials.

A reduction of the secondary electron production can also be achieved by coating the surface with a low SEY material.

The TiN coating on technological surfaces such as copper, aluminium or stainless steel substrate allows reducing δ_{max} to 1.5, see Figure 15.

Table 1: Maximum secondary electron yield of some usual chemical components.

Material	Ag	Al	Au	Polished C	Cu	Nb	Ti
δ_{max}	1.5	1	1.5	1	1.4	1.2	0.9
E_{max} (eV)	800	300	700	300	600	400	280

The non-evaporable getter (NEG) films coated on the same substrates can also reduce the maximum SEY, as it was described in Chapter 5, see Figures 5-22 and 5-23 (Oleg to check!). Thus, SEY was reduced to $\delta_{max} \approx 1.1$ with a 1-µm thick Ti-Zr-V getter film coated on copper and activated at 200 ºC [98].

Carbon coating also reduces the production of secondary electron cloud. The SEY curve of amorphous carbon coated on stainless steel deposited under Ne and Ar discharge is shown in Figure 17. A remarkable value of $\delta_{max} \leq 1$ is achieved: multipacting do not occur with such surface [99].

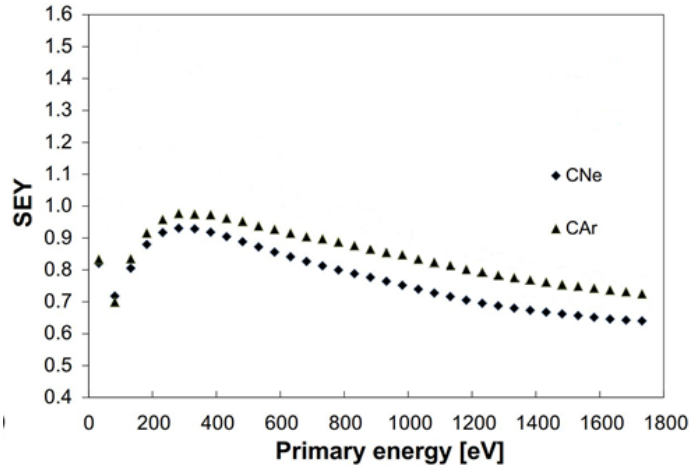

Figure 17: Secondary electron yield curves of amorphous carbon coating. Adapted from Fig.1 in Ref. [99].

8.3.5 Effect of surface roughness

The morphological aspect of a surface reduces also the secondary electron production. When the secondary electrons produced from the surface performed several collisions with the material, their chance of being absorbed is increased which results in a reduction of the net SEY.

Thus, the low SEY of as-received TiN coating happened not only due to low SE of TiN but also due to pyramidal structure created by TiN grains (due to the roughness of its surface). Indeed, thin TiN coating has a goldish colour which $\delta_{max} \approx 2.4$, whereas, the surface coated thick layer of TiN is black with $\delta_{max} \approx 1.5$,

the black aspect being attributed to the roughness of the material [100]. Thick amorphous carbon films reduce as well the SEY due to its surface roughness [99].

The production of macroscopic or microscopic structures with mechanical or laser ablation reduces further the SEY.

As illustrated in Figure 7 and Figure 18, a groove, rib or a honeycomb structure can trap the secondary electrons to reduce the effective SEY of the material [101,102]. TiN grooved with 40° opening angle and depth of 1 mm provides $\delta_{max} \approx 1.2$ [103]. Drilled copper with 75% holes of depth ~ 0.5 mm and diameter ~ 1 mm provides $\delta_{max} \approx 1.2$.

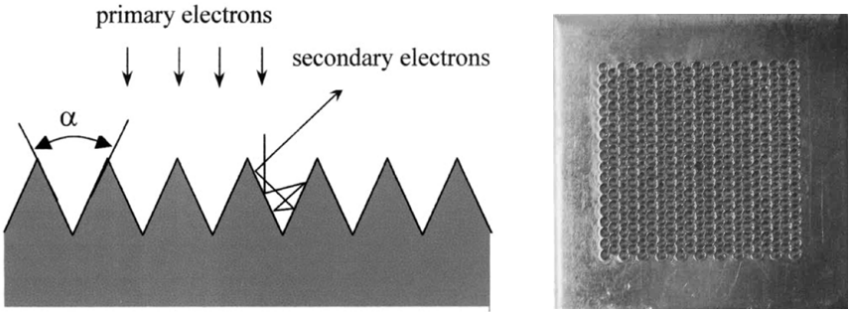

Figure 18: Surface roughness produced by grooves means (left) and drilled means (right) [101,102].

Laser ablation surface engineering (LASE) is a promising technology currently under development [77-82]. The laser ablation produces organised microstructures on a surface with SEY below 1: multipacting do not occur with such a surface. As depicted in Figure 19, left, the SEY of a laser treated Cu sample is below 1 for impinging electron energies up to 1 keV. On the right side, the scanning electron microscope image (SEM) shows the microstructure of the Cu sample where secondary electrons are trapped following successive absorptions.

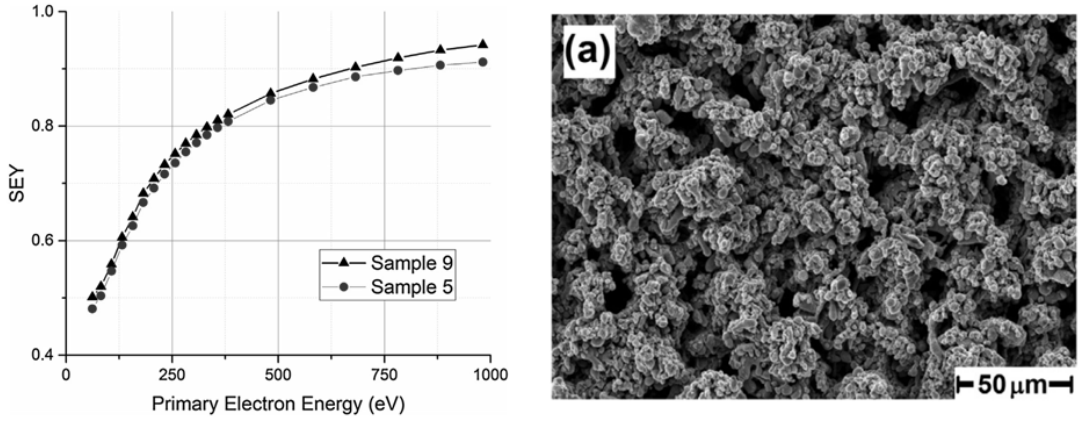

Figure 19: Secondary electron yield curves of laser treated Cu samples (left) and SEM image of "Sample 9" (right). Figs. 9 and 10 in Ref. [82].

8.3.6 "True" secondary electrons, retro-diffused electrons and reflected electrons

It must be stressed that the secondary electrons taken into account for the evaluation of the SEY in the figures above are the sum of "true" secondary electrons, retro-diffused electrons and reflected electrons [104,105]. Thus, for each point measured at a given incident primary electron kinetic energy, the emitted electrons are not mono-energetic but have rather a distribution in energy. Such electron distribution curves are highly peaked towards low energy below ~ 5 eV. However, there is always a contribution from reflected electrons. This contribution increase when decreasing the incident electron kinetic energy. For a technical surface such as copper, reflectivity above ~ 60% is measured for impinging electrons with kinetic energy below ~ 20 eV. This is illustrated in Figure 20 where the electron energy distribution curves are measured for primary electron energy ranging from 4 to 200 eV [106]. These curves are typically measured with semi-hemispherical electron analysers or low energy electron diffraction devices. The reflectivity at low electron energy of clean polycrystalline copper (*i.e.* sputtered copper) is ~ 20 % [107].

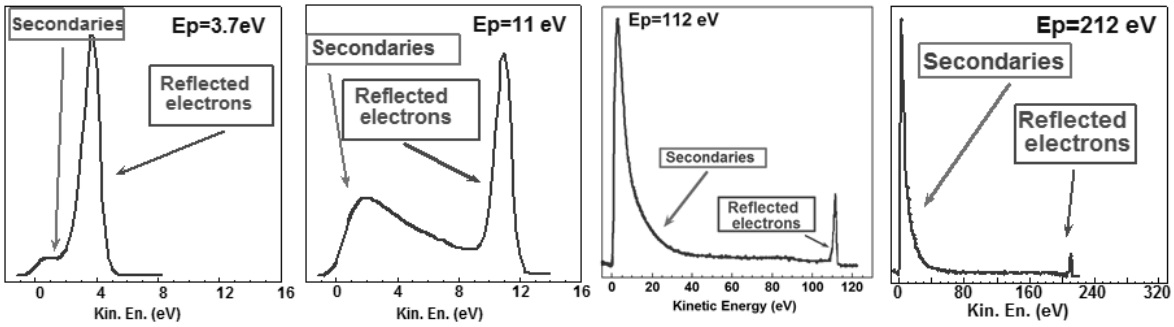

Figure 20: Electron energy distribution curves for primary electron energy ranging from 4 to 200 eV. Adapted from Fig. 1 in Ref. [106].

For the purpose of modelisation of the BIEM and electron cloud, the SEY curve can be described by the sum of true secondary electrons and reflected electrons as a function of energy of the primary impinging electrons, E_p [108, 109]:

$$\delta\left(E_p\right) = \delta_{true}\left(E_p\right) + \delta_{elastic}\left(E_p\right) \tag{8.7}$$

Where the contribution of "true" secondary electrons is given by the equation below with $s \approx 1.35$, δ_{max} the maximum of the SEY curve and E_{max} the primary energy corresponding to δ_{max}:

$$\delta_{true}\left(E_p\right) = \delta_{\max} \frac{s\dfrac{E_p}{E_{\max}}}{s - \left(1 + \dfrac{E_p}{E_{\max}}\right)^s} \ . \tag{8.8}$$

Figure 21 shows curves for Cu the obtained with Eq. (8.8) for E_{max} = 250 eV and δ_{max} = 2.2, 1.7 and 1.2. As shown, when the maximum secondary electron yield is decreased, not only the amount of multiplied electrons is decreased, but also the energy range of primary electrons that could be multiplied. When δ_{max} = 2.2, the SEY is larger than 1 for primary energy range up to 3 keV; however, when δ_{max} = 1.2, the energy range of multiplied primary electrons is reduced to the range of 100-700 eV.

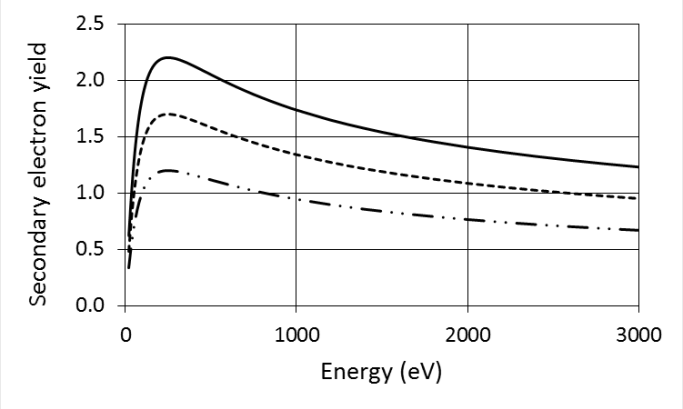

Figure 21: SEY curves of Cu, computed with Eq. (8.8), for several values of δ_{max}.

8.3.7 Effect of incident angle

When decreasing the incidence angle, the SEY increases due to the electron production closer to the surface. Introducing the angle θ with respect to the surface normal, the parameters δ_{max}, E_{max} and s may vary like [110]:

$$\delta_{max}(\theta) = \delta_{max} e^{0.4(1-\cos\theta)} \tag{8.9}$$

$$E_{max}(\theta) = E_{max} \times \left(1 + 0.7\left(1-\cos\theta\right)\right) \tag{8.10}$$

$$s(\theta) = s \times \left(1 - 0.18\left(1-\cos\theta\right)\right) \tag{8.11}$$

In magnetic field-free regions, the azimuthal distribution of the true secondary electrons follows the Beer-Lambert law but the reflection of the elastic electrons is specular.

The contribution of the "elastically" reflected electrons as a function of impinging electron energy is given by [111]:

$$\delta_{elastic}(E_P) = R_0 \left(\frac{\sqrt{E_P} - \sqrt{E_P + \varepsilon_0}}{\sqrt{E_P} + \sqrt{E_P + \varepsilon_0}} \right)^2 \tag{8.12}$$

with R_0, the reflectivity for electron impinging the surface with zero energy ($R_0 \sim 0.6$) and ε_0 the negative step potential onto which the plane-wave electron wave function is incident ($\varepsilon_0 \sim 150$ eV). Figure 22 shows the relative contribution to the total SEY, Eq. 5, of "true" and "elastic" secondary electrons. The contribution of reflected electrons is important for primary energies below 10 eV and negligible above 50 eV.

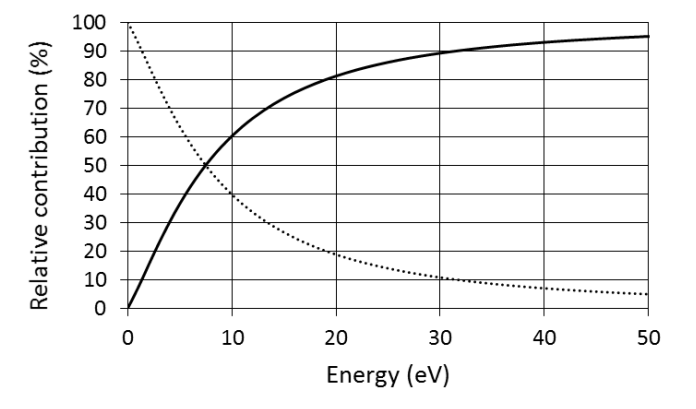

Figure 22: Relative contribution to the SEY of the "true" secondary electrons (plain) and the "elastic" secondary electrons (dot) computed from Eqs. (8.7), (8.8) and (8.12).

8.4 How the BIEM and e-cloud could affect vacuum

It was already mentioned above that electrons can be accelerated by the bunch charge, gain an energy of up to a few hundred eV and hit the vacuum chamber wall, producing not only the secondary electrons but the ESD as well.

Therefore, the gas dynamics balance equations in Chapters 5 and 6 include the gas desorption term q which consists of a few main sources: thermal desorption, PSD and ESD:

$$q = \eta_t F + \eta_\gamma \Gamma + \eta_e \Theta. \tag{8.13}$$

To estimate the BIEM and e-cloud effects on vacuum, one need to obtain

- the electron flux Θ [e^-/(s·m)],
- the (average) energy of hitting electrons $<E_e>$ [eV] which required to estimate the ESD yields,
- how well the surface was conditioned with SR and photoelectrons before the electron multipacting has been triggered on.

8.4.1 Estimation of electron energy and incident electron flux

The e-cloud modelling codes input includes a selected set of parameters such as PEY, SEY, gas density and charge particle beam characteristics. The results of the modelling provides an intensity of BIEM an e-cloud density distribution.

To calculate ESD for gas dynamics calculations we can use either the electron energy distribution, $\theta(E)$:

$$q_{ESD} = \sum_{i=1}^{N} \left(\eta_e \left(E_i \right) \Theta_i \right), \tag{8.14}$$

or the average power dissipation of multipacting electrons to the walls of vacuum chamber, $\mathscr{P}$[W/m], and the average energy of hitting electrons $<E_e>$. A use of the average electron energy, $< E_e>$, is sufficient to calculate effective electron flux Θ from the electron power $\mathscr{P}$. Considering a linear dependence of ESD yields with the electron energy in the range 50 eV < E < 1 keV (see Chapter 4),. Since the power is

$$\mathscr{P}\left[\frac{W}{m}\right] = I_e\left[\frac{A}{m}\right] U\left[V\right] = \Theta\left[\frac{e^-}{s \cdot m}\right] \left\langle E_e \right\rangle \left[eV\right], \tag{8.15}$$

then the effective electron flux per meter of vacuum chamber length can be calculated as:

$$\Theta\left[\frac{e^-}{s \cdot m}\right] = \frac{\mathscr{P}\left[\frac{W}{m}\right]}{\left\langle E_e \right\rangle \left[eV\right] q_e \left[C\right]}. \tag{8.16}$$

Then the ESD per meter of vacuum chamber can be calculated:

$$q_{ESD} = \eta_e\left(\left\langle E_e \right\rangle\right)\Theta\,. \tag{8.17}$$

If the average electron energy is not provided, it can be estimated as follows. The time-averaged electric field $\mathscr{E}$ of the beam with a Gaussian profile can be given in SI units by:

$$\mathscr{E}\left(r\right) = \frac{I}{2\pi\varepsilon_0 cr}\left(1 - e^{-\left(\frac{r}{\sigma_r}\right)^2}\right); \tag{8.18}$$

where I is the proton beam current; $\varepsilon_0 = 8.85\cdot10^{-12}$ [F/m] is the permittivity of free space; c is the speed of light in vacuum; σ_r is the rms beam size, $\sigma_r = \sqrt{\beta\varepsilon_n / \gamma}$; r is the distance from the centre of beam. However, a peak electric field (in presence of bunch of particles) is a factor T/τ higher than an average electric field value (here τ is the bunch length and T is the bunch spacing):

$$\mathscr{E}_{peak}\left(r\right) = \frac{I}{2\pi\varepsilon_0 cr}\left(1 - e^{-\left(\frac{r}{\sigma_r}\right)^2}\right)\frac{T}{\tau} \tag{8.19}$$

The electrons are accelerated toward the beam when bunch is present, and are drifting between bunches. Thus, the electron can gain the energy up to

$$E_{max} = \int_0^a \mathscr{E}_{peak}\left(r\right)dr = \frac{I}{2\pi\varepsilon_0 c}\frac{T}{\tau}\int_0^a \left(\frac{1 - e^{-\left(\frac{r}{\sigma_r}\right)^2}}{r}\right)dr\,. \tag{8.20}$$

The electron incident energy varies in the range $0 < E_e < E_{\max}$.

Integration in Eq. (8.20) can be performed numerically (see, for example, a procedure in Chapter 9) or analytically with Euler gamma functions:

$$E_{max} = \int_0^a \mathscr{E}_{peak}\left(r\right)dr = \frac{I}{4\pi\varepsilon_0 c\sigma_r}\frac{T}{\tau}\left(\log\left(\left(\frac{a}{\sigma_r}\right)^2\right) + \Gamma\left(0, \left(\frac{a}{\sigma_r}\right)^2\right) + \gamma\right); \tag{8.21}$$

here, $\Gamma(0,z)$ is the incomplete Euler gamma function, $\Gamma\left(0,z\right) = \int_z^\infty x^{-1}e^{-x}dx$; γ is Euler's constant, $\gamma \approx 0.577216$.

When the average electron energy, $\langle E\rangle$, can be calculated from numerical result or artificially set it to $\langle E_e\rangle = E_{\max}/2$.

8.4.2 Estimation of initial ESD.

The ESD yield data were discussed in Chapter 4. The ESD is proportional to ESD yield η_e, the number of electrons hitting the walls in unit of time (the electron flux Θ [e^-/(s·m)]). The ESD yield increases with incident electron energy E_e. Alike the PSD, the ESD reduces with both an integral photon and electron dose.

When there is no SR in a designed particle accelerator, then the ESD results from Chapter 4, from literature or from new dedicated experiments are applicable directly.

In a presence of SR, the beam chamber is conditioned (or scrubbed) with direct and reflected SR, see Figure 23. The SR conditioning (or scrubbing) will reduce both PSD and ESD yields. The conditioning effect can be enhanced by photoelectrons that also bombard the area of beam chamber which is not irradiated by direct SR, however the magnetic field can redistribute or trap these photoelectrons [112,113].

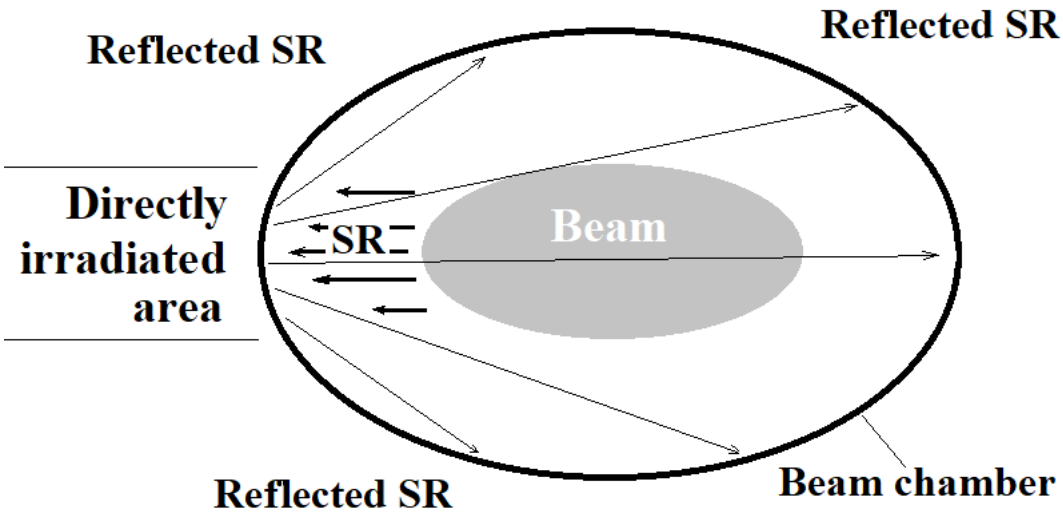

Figure 23. A vacuum chamber irradiated with direct and reflected SR.

Most commonly, the start-up scenario of the machine allows sufficient time for tuning and commissioning the machine. This means that machine runs with low beam current when SR is emitted, irradiating and conditioning the beam chamber walls, but the beam parameters are below the BIEM threshold. After some dose, the conditioning effect is not uniform neither along the beam path (see Figs. 4.31 - 4.33 in Chapter 4) nor around the beam pipe cross section, where the area directly irradiated by SR has been conditioned more intensively than other parts irradiated by reflected SR.

Thus, after reaching the BIEM threshold in the machines with SR, the initial ESD must be lower than in the machines without SR, the main problem is to estimate how strong this effect is.

As a very simplistic estimation one can use an assumption that the ESD yield (for any fixed electron energy) will be reduced with SR photon dose proportionally PSD yield, i.e. when PSD yield was reduced with SR conditioning by a factor 100, then it is reasonable to expect that ESD yield may also be reduced by a factor 100. That means that the lower the SR photon flux at the surface, the higher the initial ESD yields will be when the BIEM is triggered on, *i.e.* the highest ESD yields will be expected at the locations where there is the lowest SR intensity or no SR.

Then the terms in Eq. (8.13) can be compared to each other. If ESD is comparable or larger than the thermal and PSD, then in the gas dynamic model the significant attention should be paid to the ESD term, $\eta_e\Theta$, to check how much the gas density will increase due to BIEM. The pressure profile may dramatically change, and optimum pumping arrangement for PSD may become not ideal to cope with ESD.

One should pay attention that electron energy depends on beam and beam train parameters. Beam current may increase by increasing a number of bunches or/and by increasing a number of particles in each bunch.

- Increasing a number of bunches increases the electron flux Θ but does not affect the average energy of hitting electrons E_e, thus cause a linear increase in ESD.
- Increasing a number of particles in each bunch increases the average energy of hitting electrons E_e, which lead to higher ESD yield and may also result in higher SEY (for $E_e < E_{max}$, E_{max} = 150-650 eV for flat surfaces and E_{max} = 900-1000 eV for rough surfaces) which in turn lead to a higher electron flux Θ. In this case, the ESD may increase with beam current stringer than linear.

The ESD can significantly increase the gas density in the beam vacuum chamber; a higher gas density, in its turn, will increase gas ionisation rate by the beam particles, contributing into electron production for the e-cloud build up and change e-cloud density to unacceptably high value.

That should be considered during the vacuum system design (to provide better pumping or apply different BIEM and e-cloud mitigation techniques) and machine conditioning scenario. Such work was reported, for example, for LHC [114] and ILC [44].

8.5 BIEM and e-cloud observation in machines

8.5.1 Measurements in machines

The study and characterisation of BIEM and electron cloud in machine is obviously of great importance during the design phase of a machine and during its commissioning and operating periods. Many observables, which can be used, by the engineers and scientists for the analysis of BIEM and electron cloud are available in the control room. They can be related to the measurement of beam properties such as the beam and bunch current lifetimes, emittance growth, beam instabilities (usually in the vertical plane since the majority of a synchrotron is built of dipole magnet), energy and particle losses etc. This information is mainly available via specific beam instrumentation systems. The impact of BIEM and electron cloud can also be observed with other technical systems such as pressure rise in a vacuum system, energy deposition on a cryogenic system, beam energy loss compensated by the radio-frequency system etc.

Figure 24 shows a typical signature of electron cloud observed with the CERN Large Hadron Collider (LHC) at injection energy, 450 GeV, during a beam conditioning campaign. During this run, the machine was filled with 1596 bunches in both beams, B1 & B2. After extraction from the Proton Synchrotron injector (PS), the proton bunches are separated by 25 ns and grouped into a batch of 72 bunches each. Two batches are then injected from the PS into the Super Proton Synchrotron (SPS) to form a train. Then, 12 bunches are injected into the LHC followed by 11 trains of 144 bunches each. As shown by the fast beam current transformer, the bunch intensity is drastically reduced along each batch from 1.2×10^{11} proton per bunch (the nominal value) to 5×10^{10} proton per bunch. This reduction is due to the presence of an electron cloud into the LHC ring as

supported by the measurement of a heat load onto the 5-20 K cryogenic system of ~ 0.5 W/m per aperture (~ 22 kW around the ring!). To be noticed, in the lower plot for B2, is the smaller reduction of bunch intensity in the last three freshly injected trains.

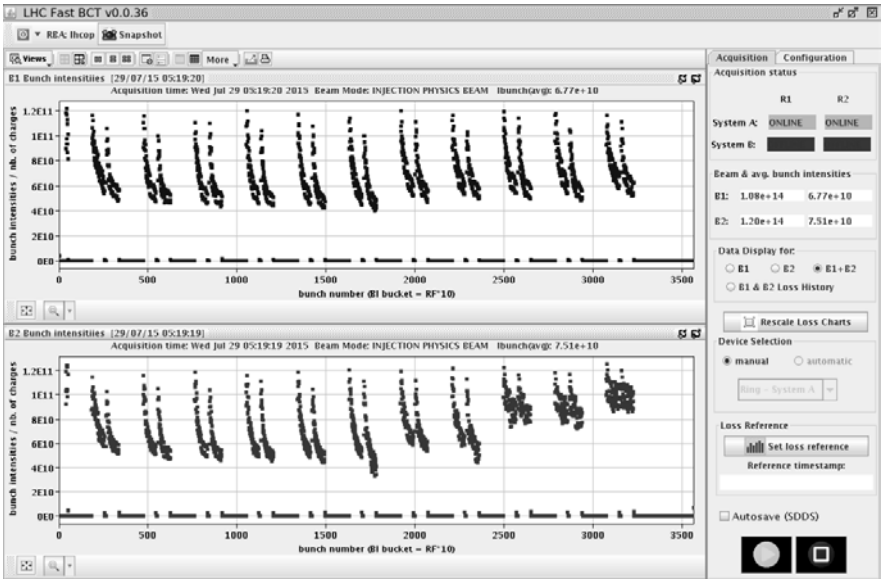

Figure 24: A typical signature of electron cloud observed on a bunch intensity fixed display of the CERN Large Hadron Collider (fill 4088, 29/7/2015).

The impact of BIEM and electron cloud can be seen on the beam emittance as shown in Figure 25. Due to the dipole field, the emittance blow-up is limited to the vertical plane (lower plots). Along the batch, the first bunches are not affected by the electron cloud but rather the ones at the end producing a typical triangular shape along each train. To be noticed also, is the absence of vertical emittance blow-up for last three freshly injected trains into B2.

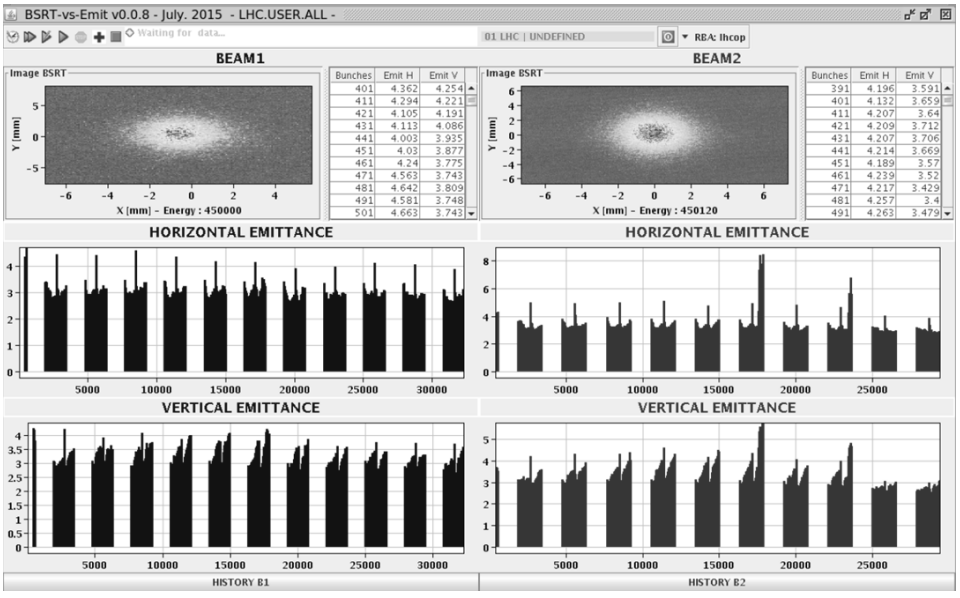

Figure 25: A typical signature of electron cloud observed on a horizontal and vertical emittance fixed display of the CERN Large Hadron Collider (fill 4088, 29/7/2015).

8.5.1.1. Vacuum pressure

The observation of BIEM and electron cloud is usually associated with a pressure increase. Depending on the electron flux to the wall, the kinetic energy of the bombarding electrons and the nature of the surface, the observed pressure increase can significantly vary. Moreover, since the BIEM is a nonlinear mechanism, the pressure increase usually changes with the beam structure from which a threshold is a typical signature. Figure 26 shows the pressure threshold observed in PEP-II due to BIEM in the vacuum chamber [115].

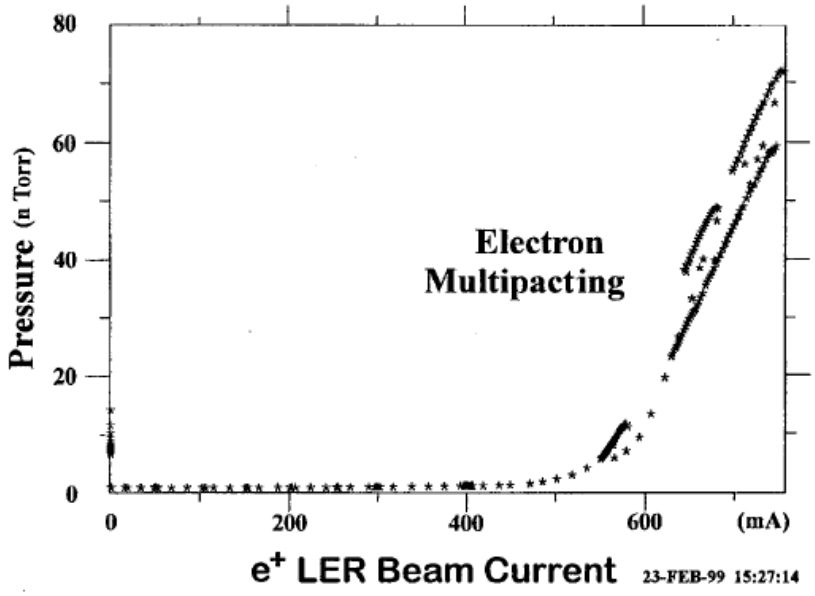

Figure 26: A typical non-linear pressure rise due to BIEM in a vacuum chamber. Fig. 4 in Ref. [115].

The BIEM and electron cloud mechanism is a strong function of the beam structure, therefore strong impact on the associated pressure rise can be observed [20]. Below a given bunch intensity, BIEM cannot be triggered due to the low energy electrons. So, in the case the gas dynamics is not dominated by other desorption processes (induced by *e.g.* photons or ions), there is no or little pressure increase. Increasing further the bunch intensity, above a given threshold, a sudden pressure increases appears due to the ESD induced by the BIEM process. If the bunch intensity is kept constant but the amount of bunches is increased, the pressure increases linearly with the number of bunches. On the other hand, if the distance between bunches is increased, the pressure rise associated to the BIEM is reduced. However, large time lag between bunches (a few 10 μs) are needed to clear completely the BIEM thereby the associated pressure rise. A much better mean than increasing the bunch distance to clear the associated pressure rise in magnetic field-free region is the wrapping of a solenoid around the vacuum chamber. Figure 27, left, shows a solenoid wrapped around the LHC beam pipe. During the LHC commissioning, as shown on the ride side of the Figure, a pressure increase up to 10^{-8} mbar was observed around the experimental areas despite the distance between the bunches was 150 ns. Since, the two beams circulates in opposite direction in the common beam pipe, the effective distance between the

bunches is reduced at specific locations. When applying a solenoidal field of 20 Gauss, this pressure increase was reduced in the 10^{-10} mbar range. The observed pressure reduction was due to the suppression of BIEM. However, it must be stressed that, despite this method is highly effective to suppress the BIEM, it does not affect the surface state of the vacuum chamber itself. Therefore, in the event the solenoidal field is switch off, the BIEM and the associated pressure rise appears again.

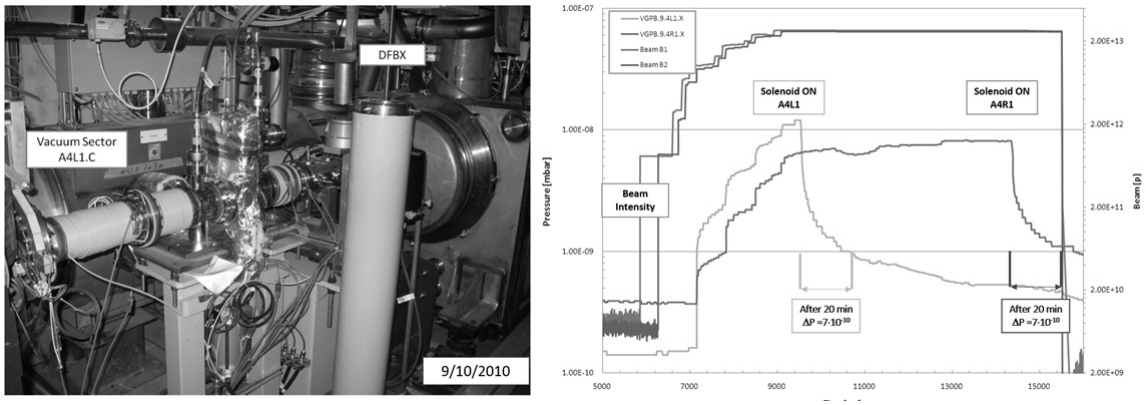

Figure 27: Left, a solenoid wrapped around the LHC beam pipe, right, observed pressure reduction when a solenoidal field of 20 Gauss is applied. Fig. 7 in Ref. [20].

8.5.1.2. Vacuum chamber wall properties

In the last decades, several specific diagnostics tools have being designed to the objective of studying in detail, not only the impact of BIEM and electron cloud on the beam itself but also the interaction of the phenomena with the vacuum surface itself.

The exposure of different type of sample to the irradiation of direct synchrotron radiation or electrons was realised in several laboratories around the world [61,116, 117, 118, 119, 120]. These studies allowed monitoring in detail the variation of important surface parameters for the understanding of the BIEM and electron cloud such as the SEY, the photon reflectivity and the PEY.

Figure 28 show a typical arrangement of such a system for the *in-situ* measurement of SEY [116]. During operation the Cu sample in placed on the side of the wall and the beam is let circulated (in this case, it is a synchrotron radiation beam). When the machine is stopped. The sample can be moved towards the SEY monitor for the measurement. During each SEY measurement, electrons from the gun bombard the sample with kinetic energy from 10 eV to 3 keV. The accumulated dose is of the order of 1 nC/cm^2 in such a way that any reduction of the SEY due to electron gun bombardment during the measurement process can be neglected. From such a device, the SEY curve is obtained by the simultaneous measurement of the drain current, I_D, on the sample which is biaised negatively in the range of – 50 to - 90 V in order to expel secondary electrons and by the measurement of the current of secondary electrons collected on a Faraday cup (or Cage), I_C, biased positively to attract electrons and placed in front of the sample. The SEY is then given by Eq. (8.5) above.

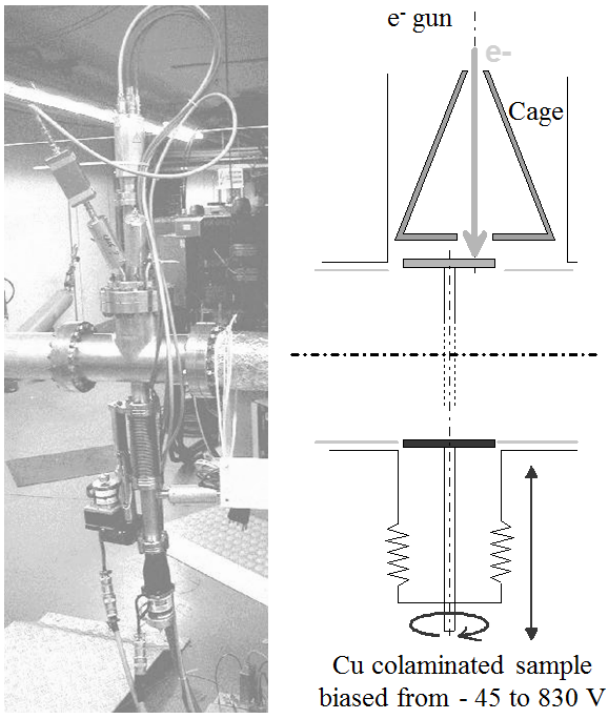

Figure 28: A set-up for *in-situ* measurement of SEY, on the bottom part, a translator exposes the sample to the electron cloud or to the SEY measurement device located on the upper part. Fig. 3 in Ref. [116].

Figure 29 shows the result of beam exposure to technical surfaces of accelerator machines. The left side presents a network of SEY curves as a function of the dose of the incident particle. In this case, a CERN Large Hadron Collider Cu colaminated type sample was exposed to photoelectrons produced by synchrotron radiation and accelerated towards the sample to 100 eV [116]. The right side shows the SEY curves of a TiN coated sample exposed to the photoelectrons and electron cloud generated during two months by the positron beam of the PEP-II low energy ring (LER). The accumulated electron dose was estimated to be ~40 mC/mm^2 [118]. In both cases, a reduction of the SEY curve under conditioning is noticed. In the laboratory, similar modifications of the SEY curve were also observed when directly bombarding the sample with electrons produced with a gun [54, 97].

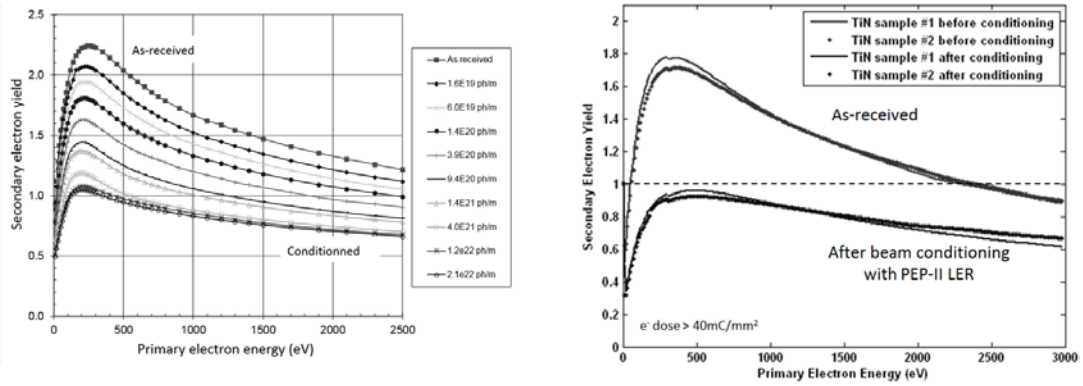

Figure 29: Left, reduction of the SEY curve as a function of photon dose when photoelectrons are accelerated to 100 V [116], right, reduction of the SEY curve after 2 months operation of the PEP-II LER. Fig. 8 in Ref. [118].

A typical plot of the maximum of the SEY during beam conditioning is shown in Figure 30. In this particular case, the photoelectrons produced on the horizontal plane by the incident synchrotron radiation were accelerated towards the unbaked Cu colaminated sample obtained from LHC beam screen material. Doing so, any artefact, due to the presence of an electron gun irradiating directly a sample (which might be the case when performing a similar measurement in the laboratory) is avoided. It is shown that the maximum of the SEY curve decrease as a function of electron dose. A value of $\delta_{max} \approx 1.2$ being reached after an electron dose of ~ 10 mC/mm^2. A closer look at this Figure indicates that the conditioning efficiency varies with the beam energy. The reduction of the maximum SEY is attributed to the graphitization of the native oxide and carbide layers, as demonstrated in a dedicated X-Ray Photoelectron Spectroscopy study. In this study the conversion of the C^{1s} core shell electrons from sp3 to sp2 was pointed-out together with a higher conditioning efficiency for electrons with kinetic energy larger than 50 eV [54, 121]. Indeed, pure sp2 Carbon (or Highly-Oriented Pyrolytic Graphite) has $\delta_{max} \approx 1$.

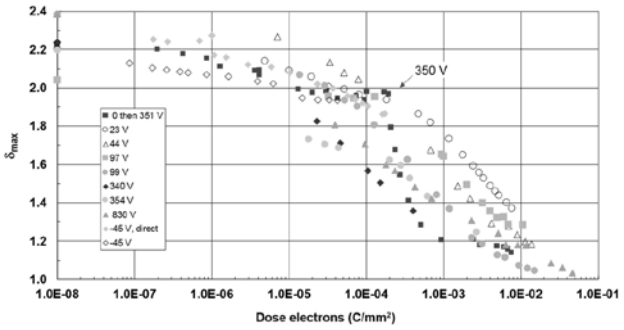

Figure 30: Reduction of the maximum of the SEY curve as a function of electron dose. Fig. 4 in Ref. [116].

From these measurements, the SEY curves were fitted by equation (14) according to equations (5) and (2). The result is depicted in Figure 31 for Cu-colaminated where the as-received and conditioned SEY curves are shown on the left and right side respectively. The error bars are defined by 3 standard deviations across the different measured samples.

$$\delta(E) = \delta_{\max} \frac{E}{E_{\max}} \frac{s}{s - 1 + \left(\frac{E}{E_{\max}}\right)^2} + a \exp\left(-\frac{E^2}{2\sigma^2}\right). \qquad (8.22)$$

Table 2 shows the result of the fitting process across five samples measured in the as-received and conditioned state. It can be seen that the conditioning process could induce a slight modification of the parameters possibly due to the graphitisation of the surface.

Table 2: Parameters for the description of the SEY curve of as-received and conditioned Cu-colaminated material.

State	δ_{max}	E_{max}(eV)	s	a	σ (eV)
as-received	2.24	220	1.401	0.560	36.8
conditioned	1.18	200	1.329	0.360	27.0

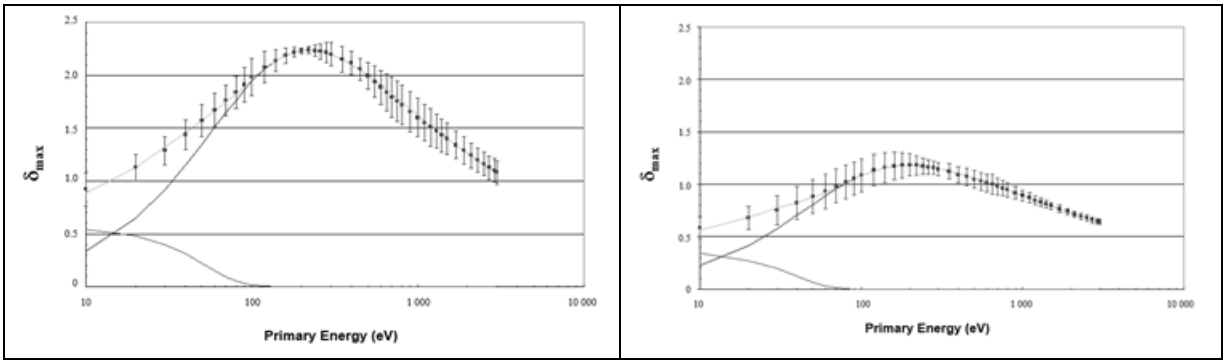

Figure 31: Left, fit to as-received Cu-colaminated sample, right, fit to conditioned Cu-colaminated sample. Fig. 5 in Ref. [116].

8.5.1.3. Specific tools for BIEM and electron cloud observation

Beside the characterisation of SEY and PEY surface parameters with dedicated devices, instruments designed to observed the BIEM and electron cloud have been developed and installed in numerous machine around the world [122, 123, 124, 125, 120, 126, 127, 128, 129, 130, 131]. Most of the instruments are based on the electron flux measurement at the vacuum chamber wall in a way to derive properties of the electron cloud. In this section, we will discuss only a few fundamentals instruments, which can be easily integrated in a vacuum system.

The simplest detector is a button pick-up (of a few 10 mm diameter) which allows the measurement of an electron current. When directly facing the beam, the pick-up is non-shielded. A wideband beam signal can be recorded at a scope. This signal indicates the presence of a beam and can be used as a trigger if needed. When shielded from the beam, the pick-up measures a current proportional to the electron cloud density. Such pick-ups are installed behind a grounded RF shield made of slots or round holes with size in the mm range. Typical transparency of the RF shield is in the range 10-40%, a compromise between the electron collection efficiency and induced perturbation on the BIEM and electron cloud. The button pick-up is positively biased in order to collect the secondary electrons produced at the button by the incoming electrons originating from the electron cloud. About +50 V is applied in practice to cancel the effect on the measured current due to secondary electrons produced at the button pick-up. Figure 32 shows on the left side a shielded button pick-up, and on the right side, a signal induced by the passage of the beam in front of a non-shielded pick-up (stripline) and a shielded pick-up (BPU2) signal induced by an electron cloud [132, 128]. In this example, the distance between successive bunches can be measured (25 ns) and the number of bunches needed to reach a quasi-equilibrium for the electron cloud is 15. In steady state, collected electron current are typically in the range 0.1 -10 μA.

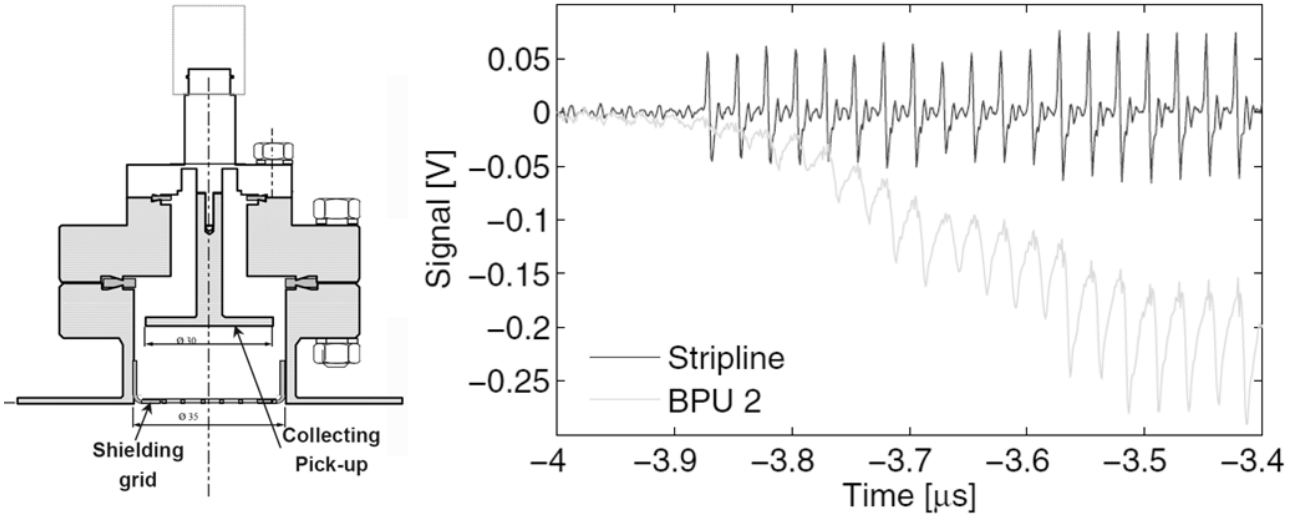

Figure 32: Left, shielded button pick-up, right, typical signal measured with a scope at an unshielded (stripline) and shielded (BPU2) button pick-up [132, 128].

Another important instrument is the Retarding Field Analyser (RFA), see Figure 33, left [133]. This instrument allows measuring the energy spectra of the electrons extracted from the electron cloud. In this case, a retarding voltage is inserted between the grounded RF shield connected to the vacuum chamber wall and the collector held at ~ +50 V. When the voltage of the analysing grid is set at a potential Vg, only the electrons whose energy is larger than Vg can cross the grid and reach the collector. During the measurement, the voltage of the analysing grid is sweep from 0 V to ~ - 500 V and the collected current is differentiated with respect to the grid voltage to obtain the electron energy spectra. In order to reduce the noise induced by the capacitive coupling between the variable voltage grid and the collector, a grid held at ground can be placed around the collector. For further noise reduction, another grounded grid can be placed between the vacuum chamber's RF shield and the retarding grid. Typical transparencies of mesh grids range from 50 to 90 %. In upgraded versions, the collector is replaced by a multi-channel plate to increase the detection sensitivity. The energy resolution of the electron spectra can also be upgraded by adding a fifth grid and using an etherodine technique similar to the one used in LEED technology to perform Auger studies [134]. In all cases, when all the grids are ground, the instrument can be used in electron current detection mode in a similar way to a shielded button pick-up. Figure 33 right, shows a typical electron energy distribution measured by a RFA exposed to an electron cloud. The distribution is peaked at low energy (~ 5 eV) and most of the electrons have an energy below 50 eV. Finally, when operating the RFA at large negative voltage (~ - 1 kV) *i.e.* detecting electrons kicked near the beam, the device can also be used to estimate the electron cloud density around the beam [130]. One must stress that this last mode of detection is of paramount importance for the machine designer since above a given electron cloud density threshold, in the range of 10^{10}-10^{12} e/m^3, an accelerator machine can be strongly unstable.

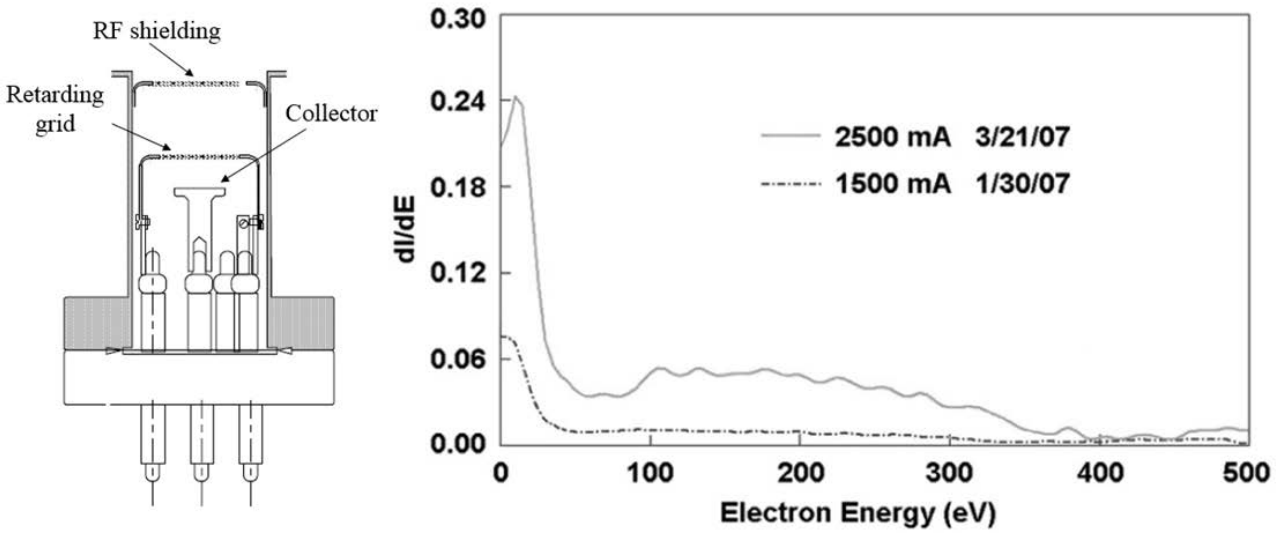

Figure 33: Left, retarding Field Analyser and, right, electron energy distribution of an electron cloud [133, 118].

As explained previously, the BIEM and electron cloud are sensitive to magnetic fields. For this reason, specific diagnostic tools have been designed to collect electron current with a spatial resolution. A typical detector is made of ~ 1 mm width Cu strips. These strips were deposited on an insulating substrate *e.g.* Macor™ or a lithographed Kapton foil with ~ 1 mm pitch. Typical collected current range from 20 nA to 20 μA [135]. Figure 34 shows typical electron current signals obtained with a multi-strip detector [132,136]. In this case, the detectors are placed in the lower part of the vacuum chamber. As shown, a spatial resolution in the mm range can be achieved. The signal measured in a vertical dipole field is shown on the left side for 9 10^{10} particle per bunch. Above ~20 Gs, the electrons are guided along the magnetic field lines. At low bunch current, the electron signal is centred in the vacuum chamber. Above ~ 5 10^{10} particle per bunch two stripes appears. The distance between the two signals is a function of the bunch current. The larger the bunch current, the larger the kick received by the electron is. Increasing further the bunch density above ~ 1.3 10^{10} particle per bunch, a third stripe appears in the centre of the vacuum chamber. Therefore, in a dipole field, the electron bombards the vacuum chambers in the horizontal and vertical plane at four distinct positions, which are a function of the bunch density. In the CERN Large Hadron Collider, the two stripes are separated by 20 mm with nominal bunch density (1.1×10^{10} protons/bunch). The signal measured in a quadruple field is shown on the right side where only the lower part of the vacuum chamber is shown. In this case, the electrons are also guided along the magnetic field lines. Thus, the electrons bombard the vacuum chamber walls at four poles locations.

Others tools are available for specific studies to understand the interplay of the electron cloud with the vacuum chamber wall. A RFA coupled with a “sweeping” electrode can monitor the electron density during the bunch passage and after its passage [127,137]. Calorimetry is performed by pick-ups or liner chambers [138,139]. The study of the multipacting mechanism can be performed with resonant standing-wave coaxial set-up [140,141].

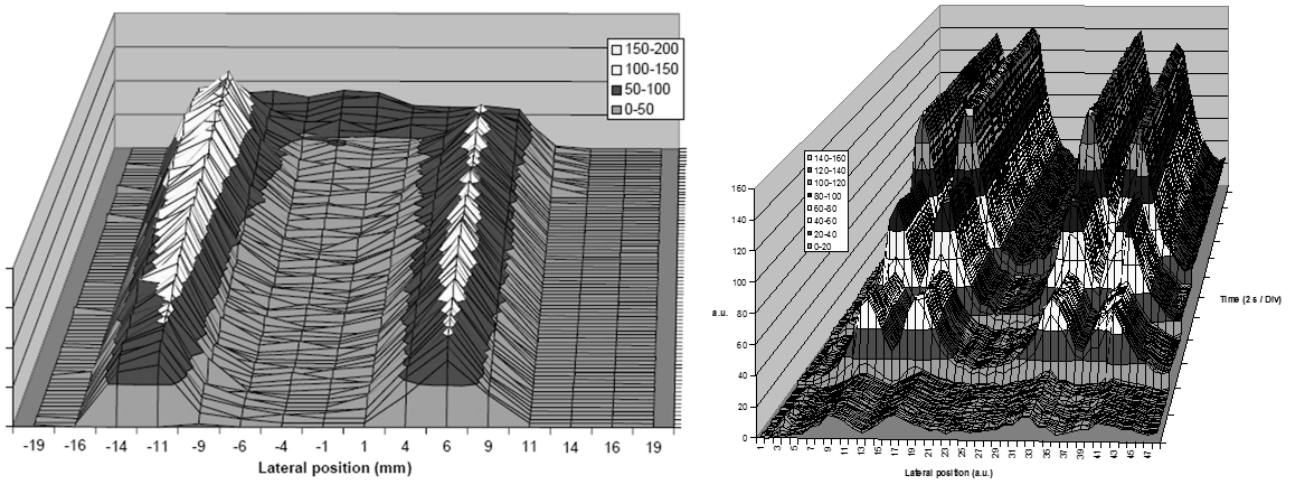

Figure 34: Typical electron current signals obtained with a multi-strip detector. On the left side, the signals are measured in a dipole field and, on the right side, measured in a quadrupole field [132,136].

8.5.2 Machines operating at cryogenic temperature

With the increasing use of superconducting magnets or RF cavities in machines around the world, there is more and more interest to understand the interplay between the vacuum system operating at cryogenic temperature and the BIEM and electron cloud. This is the case of *e.g.* RHIC, LHC and future machines such as SIS100, FCC-hh or CPPS.

8.5.2.1. Surface properties at cryogenic temperature

At cryogenic temperature, the vacuum chamber wall is usually held at temperature close to the liquid helium boiling temperature (*i.e.* 4.2 K). In this regime, as discussed in Chapter 7, the vacuum chamber wall acts as a pumping surface. Thus, gas molecules are physisorbed or condensed on the wall. Thereby, the behaviour of the vacuum system is significantly modified see *e.g.* [142,143]. The nature of the adsorbed molecules onto the surface is a function of the vacuum chamber material and its temperature. For smooth and metallic surfaces, hydrogen is adsorbed below 20 K, methane, nitrogen and carbon monoxide below 40 K, carbon dioxide below 80 K and water below 190 K. The sticking probability of the molecules is a function of the vacuum chamber material, its temperature, the surface coverage and the kinetic energy of the molecule. As it will be shown below, the surface temperature, with the presence of adsorbate on it, have significant impact on the BIEM and electron cloud trough the modification of the photoelectrons and secondary electron properties.

For surface coverage below 10^{16}-10^{17} molecules/cm^2, the PEY of a stainless steel surface held at cryogenic temperature irradiated at perpendicular incidence with synchrotron radiation of 200 eV critical energy do not differ as compared room temperature (*i.e.* ~10^{-2} e$^-$/photon). For much larger surface coverage, the PEY decrease by one order of magnitude. However, the photo-interaction with thick layers of CH_4 and CO, induce a charging of the condensate which results in a slight enhancement of the PEY [144].

At cryogenic temperature, the SEY of an as-received Cu surface is not modified as compared to room temperature. Figure 35 shows the SEY behaviour of a LHC Cu colaminated beam screen sample held at room temperature and at 9 K. As shown on the left side, the SEY at 200 eV as a function of electron dose is very similar for cryogenic and room temperature. Similarly, to Figure 30, the SEY value reduces to 1–1.2 for an accumulated dose of about 10 mC/mm^2 [145]. The SEY curve at 9K is very similar to the one at room temperature with a maximum around 250 eV [57].

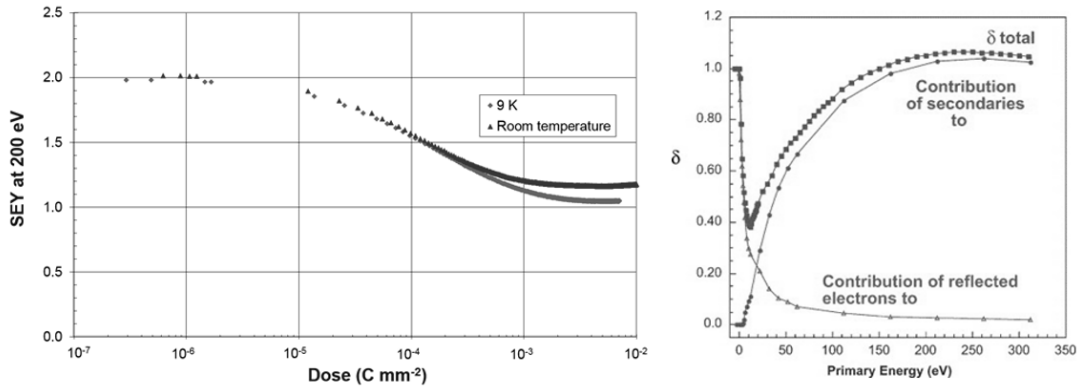

Figure 35: Left, SEY at 200 eV as a function of electron dose of a Cu sample held at room temperature and 9K, right, SEY curve of a Cu sample held at 9 K. Fig. 2 in Ref. [145] and Fig. 3 in Ref. [106].

However, when thick layers of gas are condensed onto the surface *i.e.* above a monolayer, the SEY is strongly modified. Figure 36 shows the evolution of the SEY when water is adsorbed at 77 K onto a sputter cleaned Cu baked sample [146]. The left curve shows that the water adsorption on a baked sample modifies drastically the SEY. At 200 monolayers *i.e.* a thickness of ~ 80 nm, the benefit of the bakeout (Figure 16) is fully lost and the SEY properties of an unbaked sample is recovered (Figure 15). The right curve shows the maximum SEY saturates at 2.3 above 160 monolayers of condensed water. About 10 monolayers of adsorbed water are sufficiently large to modify drastically the BIEM and electron cloud phenomena thereby deeply perturbing the operation of a machine.

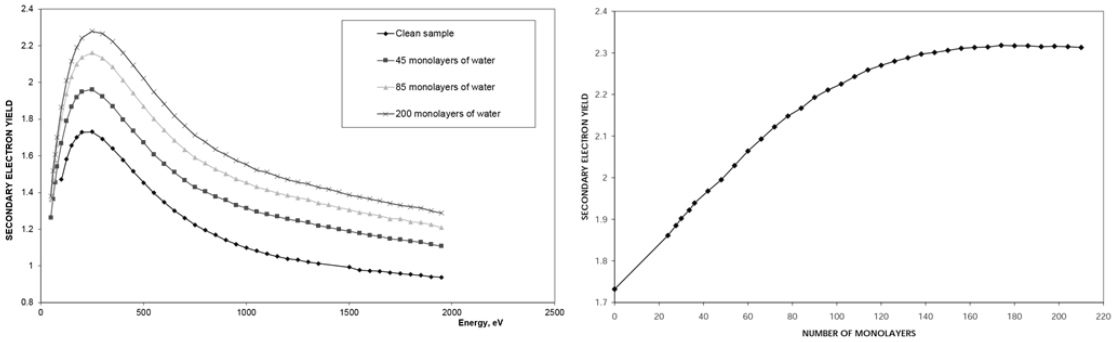

Figure 36: Left, SEY curve of water condensed on a sputter cleaned Cu baked sample held at 77 K, right, maximum SEY as a function of the number of water monolayer. Fig.6 and Fig.7 in Ref. [146**].**

In fact, as illustrated in Figure 37, only a few monolayers of any condensable gases modify the SEY curve of a surface [147]. The left curve shows the evolution of the maximum SEY of a Cu surface held at 4.7

K as a function of the amount of CO_2 and N_2 monolayers. When a monolayer is adsorbed on the surface, the maximum SEY, δ_{max}, of the as-received surface is reduced by 0.4-0.6 unit. Above 10 monolayers, the value starts to level-off around 1.7-1.9 for N_2 and CO_2. The right curve shows the evolution of the maximum SEY of condensed CO for different substrates (aluminium, copper and electro-polished copper). Again, the as received SEY, ranging from δ_{max} = 1.7 to 3, for the different technical surfaces, is modified as soon as a monolayer is adsorbed on the surface. Above 10 monolayers, the maximum SEY of condensed CO saturates at δ_{max} = 1.3. For CH_4 (not shown), the SEY saturates at δ_{max} = 1.5.

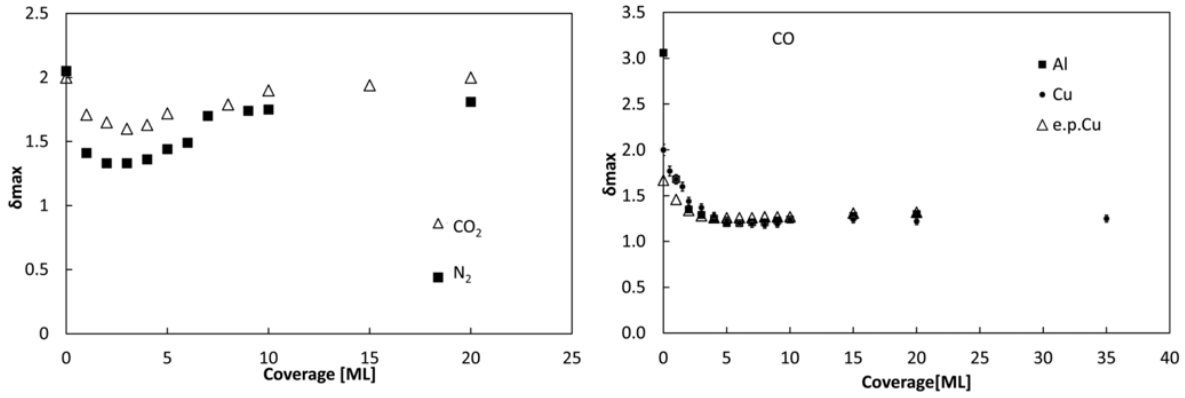

Figure 37: Left, maximum SEY of CO_2 and N_2 condensed on a Cu sample held at 4.7 K, right, maximum SEY of technical surfaces as a function of the number of CO monolayers. Fig. 9 and Fig. 12 in Ref. [147**].**

The presence of adsorbed gas onto a surface strongly modifies also the electron stimulated molecular desorption yield [148]. Figure 38 gives the electron stimulated desorption yield of H_2 and CO condensed on a baked Cu sample held at 4.2 K and bombarded by 300 eV electron [149]. For a few monolayers of gas condensed on the surface, the molecular desorption yield equals 400 H_2/e and 5 CO/e. Values for CH_4 and N_2 are similar to CO, whereas CO_2 is constant along the studied range and equals 0.3 CO_2/e. When bombarded with electron of 40 eV, the yields are roughly one order of magnitude lower.

Similarly to the case of photon irradiation, the values of electron desorption yields of condensed gases are much larger than the intrinsic desorption yield of the surface.

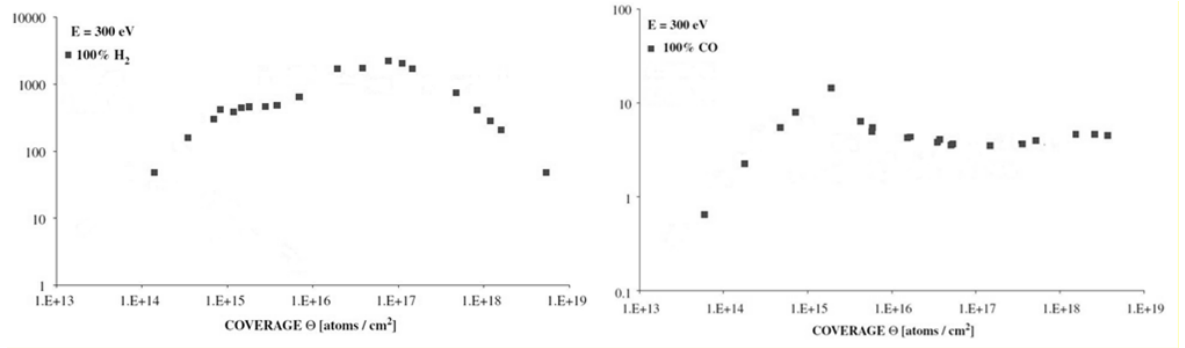

Figure 38: Electron stimulated molecular desorption yield of H_2 (left) and CO (right) condensed on a baked Cu sample held at 4.2 K. Adapted from Fig. 5 and Fig.7 of Ref. [149**].**

Thus, the adsorption of gas on a cryogenic surface can significantly modify the surface parameters of a vacuum system in such a way the pressure level, the BIEM and electron cloud phenomena are affected as illustrated in the next paragraph. When designing a vacuum system to operate at cryogenic temperature, it is therefore of primary importance that all these elements are taken into account and that all the required precautions are taken to guarantee a nominal operation of the vacuum system.

8.5.2.2. Observations with beams

To study the impact of the electron cloud on a LHC type vacuum system, the COLD bore EXperiment, COLDEX, was installed in a bypass of the CERN Super Proton Synchrotron. The cryostat is made of a 2.2 m long unbaked beam screen inserted into a cold bore (Figure 39). To mimic a LHC type beam screen, 1 % of the 67 mm inner diameter Cu beam screen is perforated with slots. The slots are shielded to protect the cold bore from heat load due to the electron cloud. During dedicated studies, the experimental set-up can be moved IN to let the LHC type beams circulating through the device. In the OUT position, the system can be prepared prior the study: the temperature of the beam screen and the cold bore can be selected and any condensable gas can be adsorbed onto the beam screen sample [150].

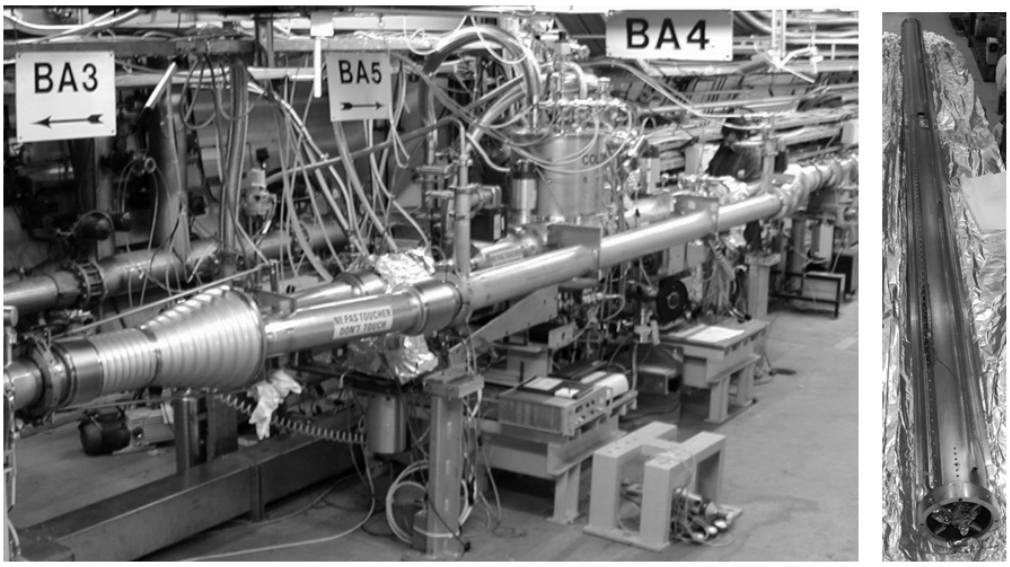

Figure 39: Left, the COLD bore EXperiment, COLDEX, installed in a bypass of the CERN SPS, right, the Cu beam screen.

The interaction of the 25 ns spaced proton bunches with the test system is monitored with total and partial pressure gauges, electron collector and calorimeters. The vacuum gauges are located in the middle of the cryostat at the top extremity of a room temperature chimney. The bottom extremity of the chimney is placed at less than one mm from the middle port of the beam screen. It allows the molecules desorbed from the cryogenic part to be measured by the vacuum gauges. Electron collectors are placed inside the chimney and behind the beam screen perforation. These collectors are shielded from the beam by a grid and by the slots of the beam screen. As shown in Figure 40, the heat load onto the beam screen (operating at T_{BS}) is measured

from the temperature sensors, T_{up} and T_{down} increase and a flow meter. Calibrated instruments are used. A heater is placed in front of the flow meter to warm up to room temperature the gaseous helium that circulates trough the beam screen. A heater wire (not shown) extended along the beam screen is used to check the calibration. With this method, beam induced heat load above 100 mW/m can be measured.

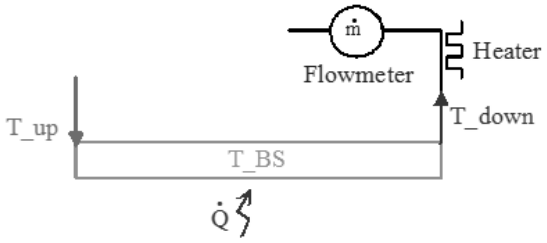

Figure 40: Schematic of the COLDEX beam screen calorimetric system.

The heat load induced by the proton beam onto the beam screen, $\dot{Q}$, is given the following equation.

$$\dot{Q} = \dot{m}\left[h_{He}\left(T_{down}\right) - h_{He}\left(T_{up}\right)\right] \qquad (8.23)$$

with $\dot{m}$, the helium mass flow, $h_{He}(T_{down})$ and $h_{He}(T_{up})$, the helium enthalpies at the temperatures of the downstream and the upstream temperature sensors respectively.

To evidence the BIEM and electron cloud phenomena, a typical test consists in studying the impact of the bunch current. As shown in Figure 41, when scanning the number a proton per bunch, a heat load is measured above a given threshold. This heat load is associated with a pressure increase and currents measured at the electron collectors. At 1.1×10^{11} proton per bunch, a typical pressure increase is a few 10^{-8} mbar with a collected current of 20 μA *i.e.* an electron activity inside the beam screen of 25 mA/m. Using simulation codes, it is shown that the SEY corresponding to the observed heat load is in the range δ_{max} = 1.1-1.2.

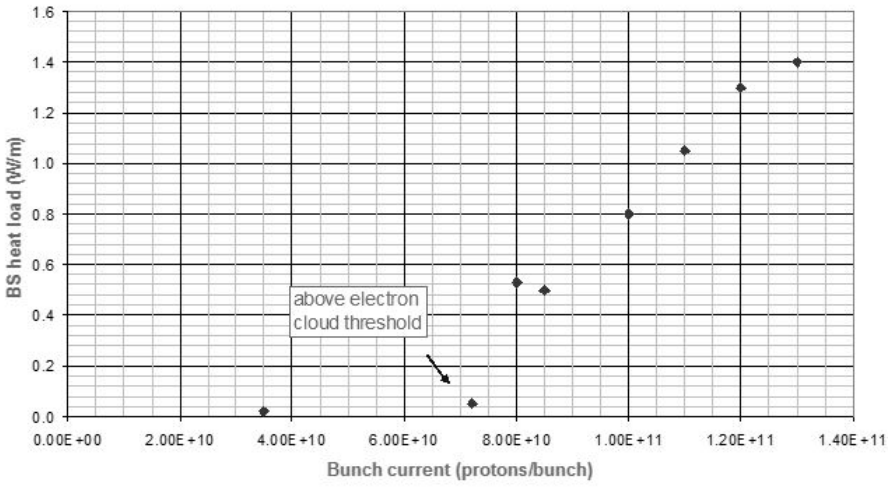

Figure 41: Evidence of a BIEM and electron cloud mechanism by observation of a threshold effect.

Other tests such as applying a solenoid field to mitigate multipacting or modifying the beam structure can also be done to demonstrate the presence of BIEM and electron cloud in a machine [20].

As explained in Chapter 7, two desorption process are observed at cryogenic temperature. The primary desorption is due to the desorption of molecules from the surface of the material, the secondary (or recycling) desorption is due to the desorption of molecules physisorbed (or condensed) on the surface of the material.

During the irradiation process, when an equilibrium pressure P_e is reached, the primary desorption yield, η, is measured from the gas flux passing through the beam screen holes:

$$\eta = \frac{GC\Delta P_e}{\Theta} \tag{8.24}$$

where $G = 2.4\ 10^{19}$ is a constant converting mbar·l to a number of molecules, C [l/s] is the conductance of the beam screen holes, ΔP_e [mbar] is the pressure increase at equilibrium and Θ [electron/s] is the electron flux.

During the whole electron bombardment process, the combination of the primary and recycling effects are observed. The sum of the primary and recycling desorption yields, η', divided by the sticking probability, α, is given by equation (17).

$$\frac{\eta + \eta'}{\alpha} = \frac{GS\Delta P}{\Theta} \tag{8.25}$$

where S [l/s] is the pumping speed of the beam screen surface and ΔP [mbar] the pressure increase expressed.

If the sticking probability is known, the recycling yield can be derived from equation (16) and (17). In absence of data, it is usually assumed that $\alpha \approx 1$.

Figure 42 shows the measured yields when the beam screen operates at 12 K and the cold bore at 3 K [150]. The left curve shows the primary electron desorption yield of hydrogen as a function of the electron dose. The yield is comparable with the results obtained at room temperature. At a dose of 10^{19} e^-/cm^2 (*i.e.* 16 mC/mm^2), the primary desorption yield of hydrogen equals 10^{-3} H_2/ e^-. The right curve shows the sum of the primary and recycling desorption yields divided by the sticking coefficient. At a dose of 10^{19} e^-/cm^2, the sum of the primary and recycling desorption yields divided by the sticking probability is in the range 10^{-3} – 10^{-1} molecules/e^-, which corresponds to a dynamic pressure in the range 10^{-9} mbar.

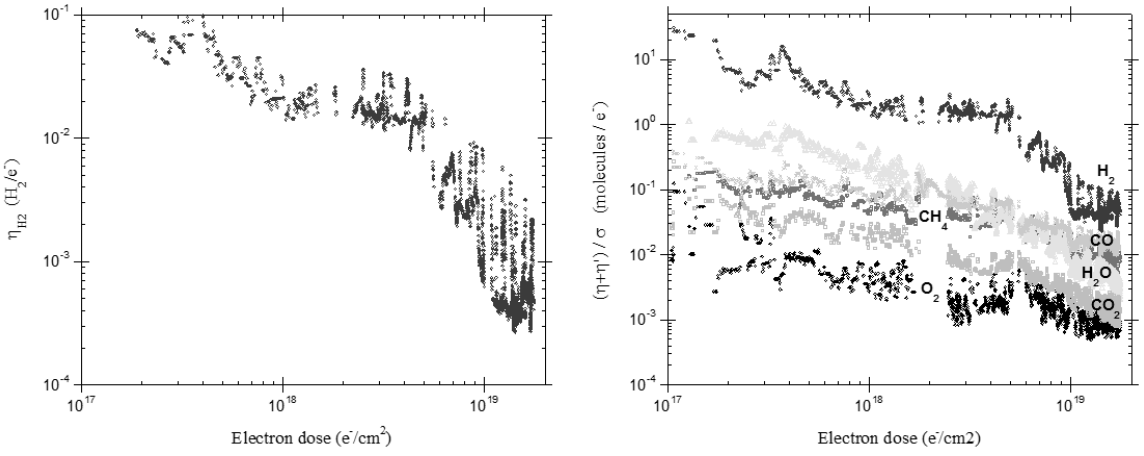

Figure 42: Left, primary electron desorption yield of hydrogen and right, sum of the primary and recycling desorption yields divided by the sticking probability of the desorbed gases as a function of the electron dose when the beam screen operates at 12 K. Fig. 7 and Fig.8 in Ref. [150].

Figure 43 shows the pressure increase due to the recycling effect when 10^{15} H_2/cm^2 (left) and 5×10^{15} CO/cm^2 (right) are condensed on the beam screen inner surface held at 5K [151]. Large pressure increases, in the range 10^{-8}-10^{-7} mbar were observed. Following equation (17), one can calculate that η'_{H2}/α = 3 H_2/ e^- and η'_{CO}/α = 0.4 CO/ e^-. A fast flushing of H_2 from the beam screen towards the cold bore within less than 0.01 A.h is indeed seen, whereas a much slower flushing (more than 0.5 A.h) for CO with a pressure level of ~ 5×10^{-9} mbar is taking place. As compared to a bare surface, the heat load increase due to such surface coverages is less than 0.1 W/m.

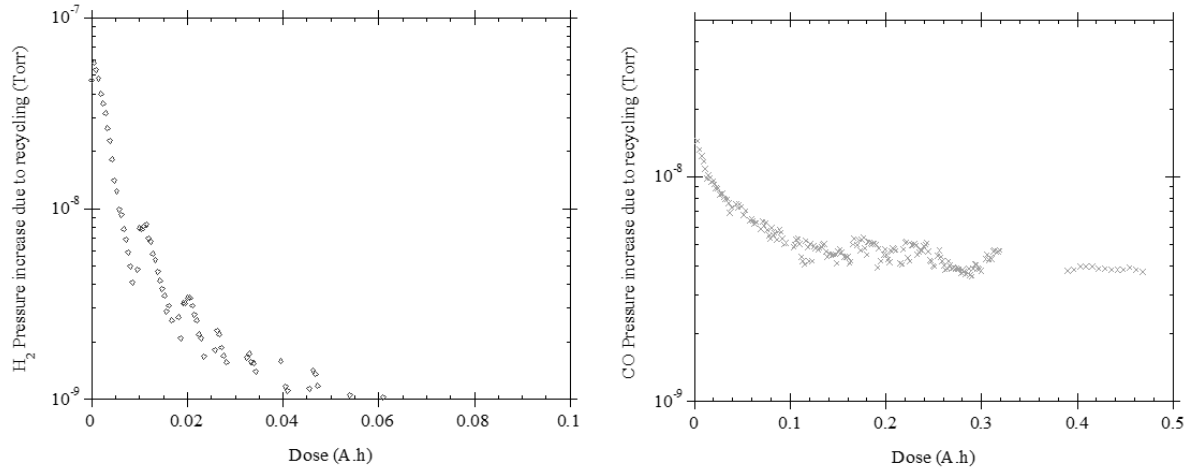

Figure 43: Pressure increase due to the recycling effect when 10^{15} H_2/cm^2 (left) and 5×10^{15} CO/cm^2 (right) are condensed on the beam screen held at 5K. Fig. 2 and Fig. 3 in Ref. [151].

However, increasing further the surface coverage of CO to 6.0×10^{16} CO/cm^2, the heat load dissipated on the beam screen rose to 6 W/m. Due to the slow flushing under electron bombardment of the CO towards the cold bore, this heat load level was maintained for a beam dose of at least 1.5 A.h. The observations reveal that thick coverages of CO results in large heat load associated with a slow flushing of gas towards the cold bore.

Figure 44 show the case of 1.5×10^{16} CO_2/cm^2 condensed onto the beam screen exposed to the electron bombardment due to BIEM and electron cloud. Under electron bombardment, the condensate is cracked into CO and O_2 molecules. As shown, the gas composition is dominated by CO which pressure level is about 7 times larger than O_2 and CO_2. It was found that η'_{CO2}/α = 0.01 CO_2/e^-. As compared to a bare surface, the heat load increase due to such surface coverage is less than 0.1 W/m [151].

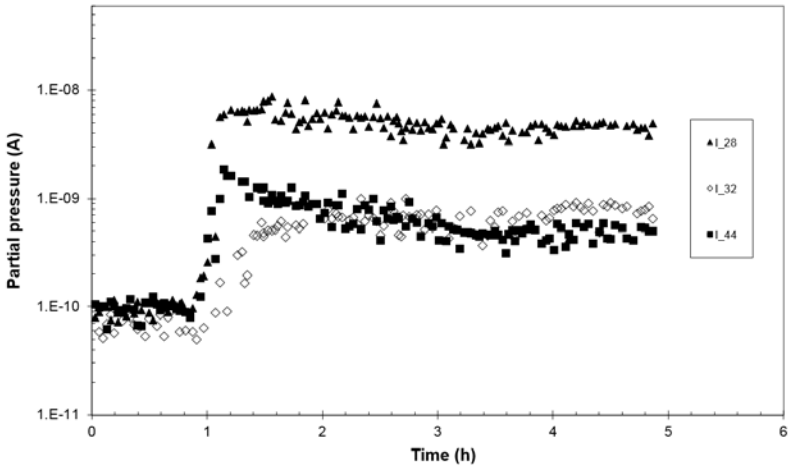

Figure 44: CO_2 cracking into CO and O_2 induced by BIEM and electron cloud. I_28, I_32 and I_44 in the legend correspond to the RGA reading at 28, 32 and 44 amu [152].

Figure 45 shows the consequence of water condensed on the beam screen when exposed to BIEM and electron cloud [153]. Due to the continuous electron bombardment, the total pressure inside the beam screen decreases during the study from 10^{-4} to 10^{-6} Pa. However, during the first phase (before 100 h), the heat load increases up to 8 W/m while the beam screen was maintained in the range 8-20 K. This increase is attributed to the electron desorption of water from the unbaked Cu beam screen which is subsequently physisorbed on the surface modifying the apparent SEY as shown in Figure 36. The accumulation of water on the surface being the consequence of a low recycling yield *i.e.* a slow flushing of the desorbed molecules by the BIEM and electron cloud towards the cold bore. Indeed, a warm-up to 240 K to remove the condensed water from the beam screen followed by a cool down (at 150 h) to nominal value results in a much lower heat load of 1 W/m.

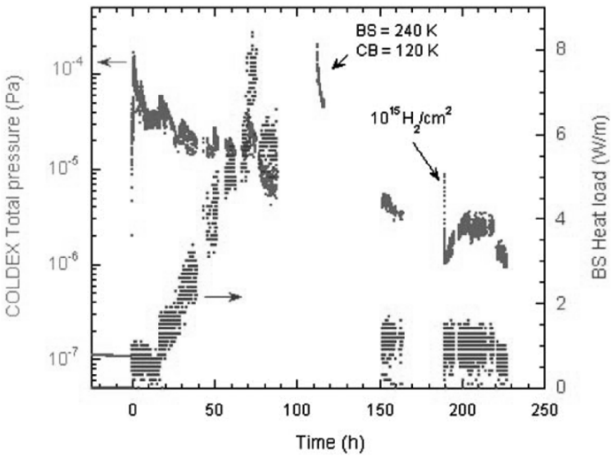

Figure 45: Total pressure and heat load due to BIEM and electron cloud. Fig. 2 in Ref. [153].

The condensation of gas can therefore modify strongly the performance of a cryogenic vacuum system subjected to BIEM and electron cloud phenomena. It can be associated with pressure rise and heat load

increase. During the design and operation phase of a cryogenic vacuum system, the vacuum engineer shall strive to minimise the amount of physisorbed (or condensed) gas on the surfaces potentially exposed to electron bombardment. The next section describes the design and operational choices made the CERN Large Hadron Collider cryogenic vacuum system to mitigate the BIEM and electron cloud.

8.5.2.3. The CERN Large Hadron Collider cryogenic vacuum system

The CERN Large Hadron Collider (LHC) is a proton storage ring bringing into collisions the particles at 14 TeV in their centre of mass. The superconducting machine is located underground in a 27 km circumference tunnel where 1232 bending dipoles of 8.33 T nominal field and 392 focusing quadrupoles of 223 T/m nominal gradient are installed. The two counter-rotating beams are located inside two-in-one magnets made of NbTi/Cu Rutherford type cables, which operates with superfluid helium at 1.9 K. The ring comprises 8 arcs of 2.7 km each, made of basic repetitive half-cell of 53.4 m length [154].

The vacuum system consists in a seamless stainless steel cold bore at 1.9 K into which is inserted a beam screen. This system is the result of several years of studies [155,156,157]. The following describes the main items (Figure 46) functions. The beam screen intercepts the beam induced heat loads from impedance, synchrotron radiation and electron cloud. As a result, the beam screens temperature along a half-cell increase from 5 to 20 K, the temperature being controlled with supercritical helium gas circulating in the cooling tubes. The racetrack shape optimises the beam aperture while leaving space for the cooling system. Sliding rings, placed every 0.75 m, ease the insertion of the 16 m long tube into the cold bore. Pumping slots are located on the top and bottom of the beam screen. The 4.4 % beam screen transparency allow to control the gas density level at the desired value. When desorbed, the molecules can be either cryosorbed on the beam screen wall or pumped through the holes towards the cold bore where the saturated vapour pressure of all gas (except helium) is negligible ($< 10^{-19}$ mbar for H_2). The transverse and longitudinal random distribution size of the rounded pumping slots minimises the electro-magnetic leakage towards the cold bore. The 75μm thick Cu layer of the inner surface of the beam screen minimises the impedance seen by the beam. In case of a transition from the superconducting to the resistive state, Eddy current circulates into the Cu material. The resulting “quench” force of a few tons are sustained by the non-magnetic stainless steel onto which Cu is colaminated. A “sawteeth” pattern on the outer side of the beam screen intercepts the synchrotron radiation at quasi-perpendicular incidence thereby reducing the photoelectron production and the forward scattering of the photons minimising the amount of electron available for BIEM. In dipole magnets, electron shields clamped on the cooling tube intercept the electrons, which circulate along the vertical field lines, protecting the cold bore from BIEM and electron cloud heat load.

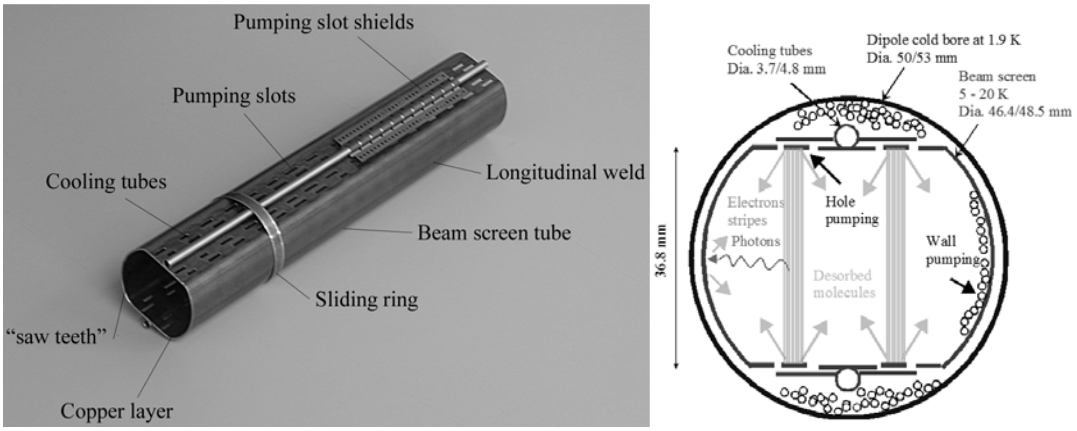

Figure 46: Picture of a LHC beam screen tube and schematic cross section of the LHC cold bore/beam screen assembly. Fig. 1 in Ref. [145].

The LHC operation started the 10th of September 2008 [158]. Unfortunately, the 19th of September 2008, an electrical default provoked the damage of several magnets, which repair took 14 months. After a thorough repair and consolidation of the vacuum system, the LHC reached its design luminosity the 26th June 2016 [159, 160, 161, **Error! Bookmark not defined.**, 162, 163, 164, 145].

The first signs of BIEM and electron cloud in the LHC vacuum system were observed in autumn 2010 during physics operation. As already explained above (Figure 27), a solenoid wrapped around the vacuum chamber demonstrated the presence of BIEM and mitigated the electron cloud build-up [**Error! Bookmark not defined.**]. Until the end of 2012, the machine mainly operated with 50 ns bunch spacing, which limited the appearance of BIEM electron cloud in the arc to dedicated studies during which the bunch spacing was reduced to 25 ns [162, 165].

After the 2013-2014 shutdown, from 2015 onwards, the LHC operated with 25 ns bunch spacing. Therefore, BIEM and electron cloud was routinely observed in the LHC arcs. Figure 47 shows the reduction of the dynamic pressure (left) and of the maximum SEY (right) observed during the first years of LHC operation when increasing the total beam intensity. Thanks to this beam conditioning, the machine could reach its design luminosity in June 2016 ready for a full operation [145].

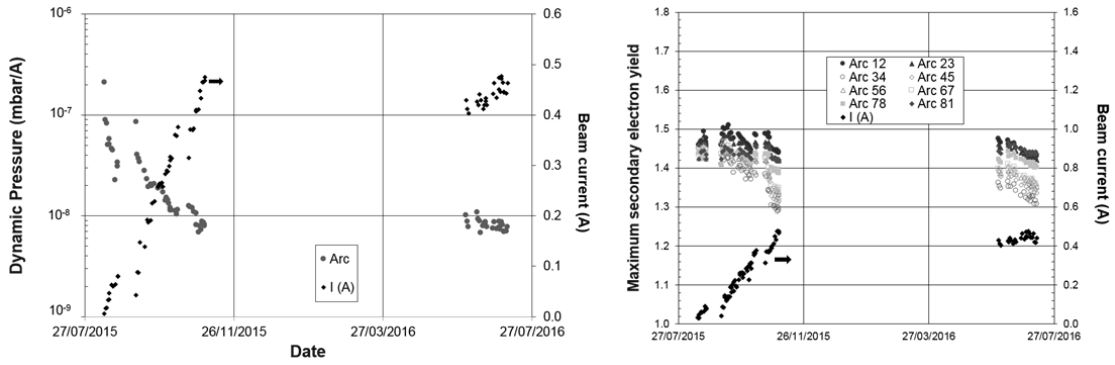

Figure 47: Left, dynamic pressure and right, maximum SEY evolution with time. Fig. 7 and Fig. 6 in Ref. [145].

However, the electron cloud phenomenon in a cryogenic machine remains highly sensitive to the surface state. In particular, the growth of gas on the cryogenic surface shall be controlled at any time. As illustrated in Figure 48 for the LHC case, pressure excursions along the cold beam pipe can occur in some circumstances. The left side shows the impact of an air leak (~ 10^{-8} mbar·l/s) into the system during a month. During this period, some air can accumulate onto the beam screen resulting in an increase of the N_2 surface coverage up to a monolayer. In this example, operating the LHC with 1.5 W/m dissipated on the beam screen by the electron cloud results in a pressure rise above the magnet quench limit. The right side of the figure illustrates the consequence of an excess of CO coverage on the beam screen. For instance, after a magnet quench, the LHC cold bore temperature is increased up to 30-40 K leading to a redistribution of the condensed gas on the surface exposed to the BIEM. Thus, without taking any particular precaution, successive quenches can occur when the machine is operated at its maximum performances. Indeed, an electron cloud dissipating 1.5 W/m on the beam screen cryogenic can trigger a magnet quench. As shown, a mitigation consists to reduce the electron flux on the vacuum chamber wall. This allows flushing slowly the excess of gas towards the cold bore without the risk triggering a quench. In this example, 20 h is needed to flush ~ 25 monolayer of gas towards the cold bore. A better solution consists in warming up the beam screen to flush thermally the excess of gas towards the cold bore or an external pumping system [166, 167].

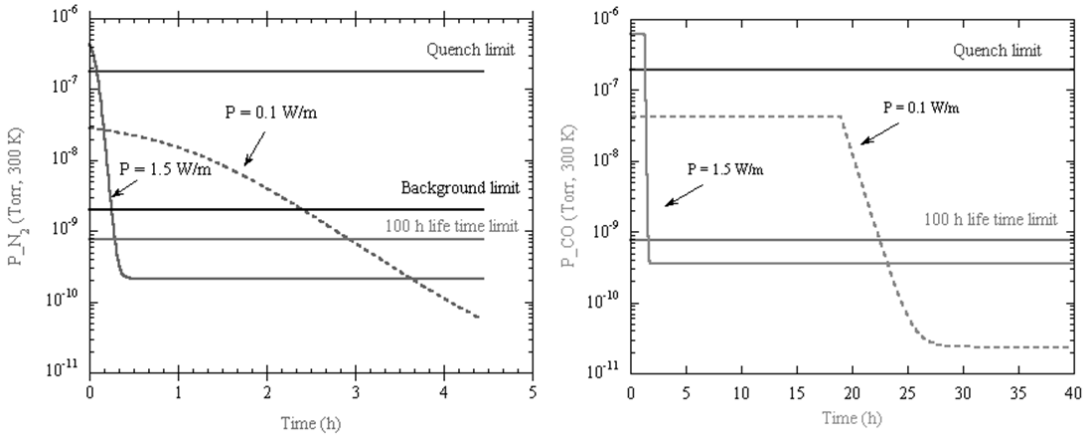

Figure 48: Vacuum transients due to an air leak (left) and due to large coverage of carbon monoxide (right). Fig. 1 in Ref. [166] and Fig. 7 in Ref. [167].

This type of event was indeed observed in the sector 16L2 of LHC where an excess of condensed gas, following an uncontrolled maintenance of the vacuum system, triggered magnet quenches and beam dumps. The solution consisted in using specific beams with longer spaces between bunches to reduce the BIEM and warming up the sector to allow a proper maintenance of the vacuum system [168].

8.6 Contribution of BIEM to vacuum stability

The effect of ion induced pressure instability is discussed in Chapter 9. Here we would like to demonstrate how BIEM may enhance this effect.

The interaction of the electron cloud with the residual gas causes the production of ions. Well-known from the vacuum expert, the hot cathode gauge, which operates in XHV and UHV regimes, uses this mechanism to measure the pressure. In this gauge, the residual gas is ionised by the emitted electrons from a filament. This gauge, for which the electron kinetic energy is set to ~100 eV, is designed to optimise its sensitivity by maximising the ion production cross section according to Figure 49 based on Data from the National Institute of Standards and Technology from atomic and molecular databases [169].

At this stage, it must be underlined that, a similar range of electron kinetic energy is achieved within accelerator vacuum system where BIEM occurs!

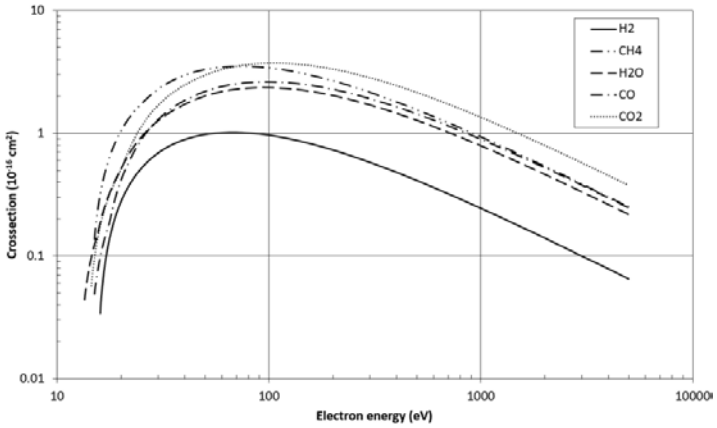

Figure 49: Electron ionisation cross section of some common gases [169].

The ion flux, I_e^+, from the residual gas ionisation process due to the electron cloud is given by:

$$I_e^+ = \sigma_e \frac{P}{k_B T} L_e I_e \tag{8.26}$$

where σ_e is the electron ionisation cross section of a given gas specie, P is the pressure, T is the temperature, L_e is the ionisation path length, I_e is the linear electron cloud flux.

In a hot cathode gauge, the typical ionisation path length is of the order of a few cm. However, in a synchrotron, this length might be significantly increased by several orders of magnitude and shall be computed for each case.

This ion production rate shall be compared to the ion flux produced by the circulating beam for *e.g.* a proton beam. In this case, the ion flux, I_p^+, is given by (19):

$$I_p^+ = \sigma_p \frac{P}{k_B T} I \tag{8.27}$$

where σ_p is the proton ionisation cross section of a given gas specie, I is the proton beam current.

Fig. 1-1 in Chapter 1 shows the electron and proton ionisation cross section for typical gas species as a function of the beam energy. This cross section depends only on the velocity of the ionising particle but neither on its charge nor on its mass. Thus,

$$\frac{I_e^+}{I_p^+} = \frac{\sigma_e L_e I_e}{\sigma_p I} \tag{8.28}$$

Proton ionisation cross sections are in the 10^{-22} m^2 range whereas electron ionisation cross sections are ~ 100 times larger. Therefore, in the case the electron ionisation path length is 1 m long and assuming a typical electron cloud flux of ~ 0.01 A/m, the contribution of the ion production rate by the electron cloud is very similar to the ion production rate of a 1 A circulating proton beam.

In the next chapter, we will develop in detail the interaction of the ions with the vacuum chamber wall and its interplay with the circulating beam. However, we will simply give here the result of the analysis including the ionisation rate by the electron cloud.

Under the combination of the (electron cloud and beam) ionisation processes and the ion bombardment of the vacuum chamber wall, the pressure, *P*, in a vacuum system obtained from the gas balance equation, is given by (21):

$$P = \frac{Q_0 + \eta_e k_B T \frac{I_e}{q_e}}{S_{eff}\left(1 - \frac{\eta_{ion}\left(\sigma_p I + \sigma_e L_e I_e\right)}{q_e}\right)} \tag{8.29}$$

where Q_o is the thermal desorption rate, η_e is the ESD yield, η_{ion} is the ISD yield, S_{eff} is the effective pumping speed.

This equation illustrates the feedback mechanism on the residual gas following the molecular desorption stimulated by the ion bombardment due to the beam-gas and electron cloud-gas ionisation processes on the residual gas. When the denominator of (21) approach zero *i.e.* when the effective pumping speed cannot cope anymore with the ion production rate, a pressure runaway appears. Assuming a linear increase of the electron cloud flux on the vacuum chamber wall with the beam current, $I_e = aI$, where a is a coefficient, then the critical current, I_c, for which the pressure runaway becomes unstable is given by (22):

$$I_c = \frac{S_{eff} q_e}{\eta_{ion}\left(\sigma_p + \sigma_e L_e\right)} \tag{8.30}$$

Thus, the presence of the electron cloud reduces the critical current of a given vacuum system. In the simple case of beam stacking in a circular machine, α=1, therefore, the critical current is divided by ~ 10 for an electron ionisation path length of 10 cm.

This phenomenon was observed in RHIC [170].

8.7 Past, present and future machines

Since BIEM and electron cloud phenomena can severely limit the operation of a storage rings, the detailed understanding of the interplay of the BIEM and electron cloud with the vacuum chamber wall is of paramount importance for the vacuum scientist. Significant progresses have been achieved over the last decades thanks to detailed studies, simulations and the development of new technologies and mitigations techniques. Table 3 gives an overview of the BIEM and electron cloud key parameters of several machines around the world, which have dealt, are dealing or will deal with BIEM and electron effects. And although further studies on e-cloud mitigation are continued, the modern state of knowledge and technologies provides sufficient confidence that the new machined can be designed and built to meet the specifications on:

- PEY and SEY to ensure operation of accelerator below the e-cloud thresholds on the e-cloud density (or the space charge);
- the BIEM power dissipation limit to ensure that cooling capacity of beam chamber of the beam screen is sufficient for keeping temperature within a design range and for the stable operation of the cryogenics;
- the gas density due to ESD is below a specified value;
- etc.

8.8 Acknowledgments

Authors would like to acknowledge Dr. Mikhail Zobov and Dr. Roberto Cimino from DAΦNE (INFN, Frascati, Italy) for the many comments and suggestions.

Table 3: Overview of BIEM and electron cloud key parameters for some past, present and future synchrotrons around the world.

	PEP-II low energy ring	KEKB low energy ring	DAΦNE	LHC	HL-LHC	SuperKEKB	ILC damping ring	FCC-hh
Particle	e+	e+	e+	p	p	e+	e+	p
Energy [GeV]	3.1	3.5	0.51	7 000	7 000	4	5	50 000
Intensity [A]	2.2	1.7	1.4	0.58	1.12	3.6	0.4	0.5
Luminosity [Hz/cm^2]	3×10^{33}	2×10^{34}	5×10^{32}	1×10^{34}	5×10^{34}	80×10^{34}	n/a	5×10^{34}
Circumference [km]	2.2	3.02	0.10	26.66	26.66	3.02	3.2	97.75
Nb of bunches	1658	1284	120	2808	2748	2500	1312	10 426
Bunch population	6×10^{10}	9×10^{10}	2×10^{10}	1.15×10^{11}	2.2×10^{11}	9×10^{10}	2×10^{10}	1×10^{11}
Bunch spacing (ns)	4.2	7	2.7	25	25	4	554	25
Bunch length (ns)	0.05	0.02	0.1	0.25	0.25	0.02	0.02	0.25
Horz./Vert. Normalised emittance [μm rad]	0.049 / 0.002	0.018 / $1.8\ 10^{-4}$	1 / 0.01	3.75	2.5	0.003 / 10^{-5}	5.5 / 0.02	2.2
Electron cloud density instability threshold [m^{-3}]	1×10^{12}	4×10^{11}	1×10^{13}	5×10^{11} at 450 GeV	1×10^{12} at 450 GeV	3×10^{11}	4×10^{10}	4×10^{10} at 3 TeV
Vacuum chamber material	Al	Cu	Al	Cu colaminated on stainless steel	Cu colaminated on stainless steel	Cu / Al	Cu	Cu colaminated on stainless steel
BIEM and electron cloud mitigation technique	antechamber, TiN coating, solenoid windings	solenoid windings	antechamber, clearing electrodes, solenoids, beam scrubbing, machine feedback	beam scrubbing, sawtooth, TiZrV coating	beam scrubbing, sawtooth, TiZrV coating, a-C coating,	TiN coating, grooves with TiN coating, clearing electrodes, solenoid windings, permanent magnets, antechamber	TiN coating, grooves with TiN coating, NEG coating, clearing electrodes, solenoid windings, antechamber	laser treated surface, antechamber, sawtooth

REFERENCES

[1] G. Budker, G. Dimov, V. Dudnikov. Experiments on production of intense proton beam by charge exchange injection method. In Proc. of the International Symposium on Electron and Positron Storage Rings, Saclay, France, 1966, Article no. VIII-6-1 (1966).
[2] G. Budker, G. Dimov and V. Dudnikov. Experimental investigation of the intense proton beam accumulation in storage ring by charge- exchange injection method, Soviet Atomic Energy, **22**, 384 (1967).
[3] G. Budker, G. Dimov, V. Dudnikov and V. Shamovsky, in Proc. of the International Conference on High Energy Accelerators, Cambridge, MA, 1967 (CEA, Cambridge, MA, 1967).
[4] J. H. Martin, R. A. Winje, R. H. Hilden, and F. E. Mills, in Proc. of the 5th International Conference on High Energy Accelerators, Frascati, 1965 (CNEN, Rome, 1966), p. 347.
[5] E.C. Raka, in Proceedings of the International Conference on High Energy Accelerators, Cambridge, MA, 1967, p. 428 (CEA, Cambridge, MA, 1967)
[6] F. Zimmermann. Review of single bunch instabilities driven by an electron cloud. Phys.Rev.ST Accel. Beams **7**, 124801 (2004).
[7] F. Zimmermann. Electron-cloud effects in past & future machines – walk through 50 years of electron-cloud studies. Conf. Proc. C **1206051**, 9-17 (2013).
[8] H. A. Grunder and G. R. Lambertson, in Proceedings of the 8th International Conference on High Energy Accelerators, Geneva, 1971 (CERN, Geneva, 1971).
[9] D. Neuffer, E. Colton, D. Fitzgerald, et al. Observations of a fast transverse instability in the PSR. Nucl. Instrum. Methods Phys. Res. Sect. A **321**, 1-12 (1992).
[10] M. Blaskiewicz, in Workshop on Instabilities of High Intensity Hadron Beams in Rings, edited by T. Roser and S. Y. Zhang, AIP Conf. Proc. No. 496 (AIP, New York, 1999).
[11] W. Fisher, J.M. Brennan, M. Blaskiewicz, and T. Satogata. Electron cloud measurements and simulations for the Brookhaven Relativistic Heavy Ion Collider. Phys. Rev. ST Accel. Beams **5**, 124401 (2002).
[12] A. Kulikov, A.S. Fisher, S. Heifets, et al. The Electron-Cloud Instability at PEP-II. In Proc. of 2001 Particle Accelerator Conference (2001), p. 1903
[13] X. Zhang et al, "Electron Cloud Studies at Tevatron and Main Injector," Proc. 2007 Particle Accelerator Conference (2007), p. 3501.
[14] V. Danilov and S. Cousineau. Accumulation of High Intensity Beam and First Observations of instabilities in the SNS Accumulator Ring. In Proc. of the ICFA HB 2006 Workshop, Tsukuba (2006).
[15] G. Dugan, M.G. Billing, K.R. Butler, J.A. Crittenden, M.J. Forster, et al. Studies at CesrTA of Electron-Cloud induced Beam Dynamics for future Damping Rings. Proc. of IPAC2012 New Orleans (2012), p. 2081.
[16] R. Calder, E. Fischer, O. Gröbner, and E. Jones, in Proceedings of the 9th International Conference on High Energy Accelerators, Stanford, 1974 (A.E.C., Washington, DC, 1975), pp. 70–74.
[17] R. Cappi, M. Giovannozzi, E. Métral, G. Métral, G. Rumolo, and F. Zimmermann. Electron cloud buildup and related instability in the CERN Protron Synchrotron. Phys. Rev. ST Accel. Beams **5**, 094401 (2002).
[18] G. Arduini, K. Cornelis, O. Gröbner, N. Hilleret, W. Hofle, J.M. Jimenez *et al*. Electron cloud: observations with LHC-type beams in the SPS. Proc. of EPAC'00, Vienna, Austria, 26-30 June 2000, p. 939 (2000).
[19] O. Dominguez, K. Li, H. Maury Cuna et al. First Electron-Cloud Studies at the Large Hadron Collider. Phys. Rev. ST Accel. Beams **16**, 011003 (2013)
[20] G. Bregliozzi, V. Baglin, P. Chiggiato, P. Cruikshank, J.M. Jimenez et *al*. Observations of electron cloud effects with the LHC vacuum system, Proc. of IPAC'11, San Sebastián, Spain, 2011, p. 1560.
[21] M. Izawa, Y. Sato, and T. Toyomasu. The Vertical Instability in a Positron Bunched Beam. Phys. Rev. Lett. **74**, 5044 (1995).
[22] H. Fukuma. 3D simulation of photoelectron cloud in KEKB LER. Proc. of ECLOUD'02, Geneva (Report No. CERN-2002-001, 2002).

[23] Y. Suetsugu, K. Shibata, T. Ishibashi, H. Fukuma, M. Tobiyama, J. Flanagan. Achievements and problems in the first commissioning of superKEKB vacuum system. J. Vac. Sci. Technol. A **35**, 03E103 (2017).
[24] R. Cimino, A. Drago, C. Vaccarezza, M. Zobov, G. Bellodi, et al. Electron cloud build-up study for DAΦNE. Proc. of PAC'05, Knoxville, Tennessee, 16-20 May 2005, p. 779 (2005).
[25] R. Wanzenberg. Observations of electron cloud phenomena at PETRA III. Proc. of ECLOUD12, 5-9 June 2012, La Biodola, Isola d'Elba, p. 89 (2012).
[26] A. Pertica and S.J. Payne. Electron cloud observations at the ISIS proton synchrotron. Proc. of ECLOUD12, 5-9 June 2012, La Biodola, Isola d'Elba, p. 237 (2012).
[27] F. Zimmermann, M. Korostelev, D. Schulte, T. Agoh, K. Yokoya. Collective effects in the CLIC damping rings. Proc. of PAC'05, Knoxville, Tennessee, 16-20 May 2005, p. 1312 (2005).
[28] H. Maury Cuna, J. Guillermo Contreras and F. Zimmermann. Simulations of electron-cloud heat load for the cold arcs of the CERN Large Hadron Collider and its high-luminosity upgrade scenarios. Phys. Rev. ST Accel. Beams **15**, 051001 (2012).
[29] J.A. Crittenden, J.V. Conway, G. Dugan, M.A. Palmer, D. L. Rubin, et al. Investigation into Electron Cloud Effects in the ILC Damping Ring Design. Proc. of IPAC2012 New Orleans (2012), p. 1963.
[30] M. Pivi, T. Raubenheimer, L. Wang, R. Wanzenberg, A. Wolski, F. Zimmermann. Simulation of the electron cloud for various configurations of a damping ring for the ILC. EPAC'06, Edinburgh, Scotland, June 2006, p. 2958 (2006).
[31] F. Zimmermann *et al*. Beam dynamics issues in the FCC. Proc. of HB2016, Malmö, Sweden, 3-8 July 2016, p. 373, (2016).
[32] E. Belli, P. Costa Pinto, G. Rumolo, T. Sinkovits, M. Taborelli *et al.* Electron cloud studies in FCC-ee. Proc. IPAC2018, Vancouver, Canada, April-29 to May, 4, 2018, p. 374 (2018).
[33] F. Zimmermann. Horizontal Instability in the KEKB HER. KEK, 19Oct -1Nov 2002 and 16-29 March 2003.
[34] B. Feng, C. Huang, V. Decyk, W.B. Mori, G.H. Hoffstaetter, P. Muggli and T. Katsouleas. Simulation of electron cloud effects on electron beam at ERL with pipelined QuickPIC. AIP Conference Proceedings **1086**, 340 (2009); https://doi.org/10.1063/1.3080929.
[35] J.A. Crittenden, J.R. Calvey, G. Dugan, J.A. Livezey, D.L. Kreinick, et al. Studies of the Effects of Electron Cloud Formation on Beam Dynamics at CesrTA. Proc. PAC'09, 4-8 May 2009, Vancouver, British Columbia, Canada, p. 106 (2009).
[36] U. Iriso, S. Casalbuoni, G. Rumolo, F. Zimmermann. Electron Cloud Simulations for ANKA. Proc. PAC'09, 4-8 May 2009, Vancouver, British Columbia, Canada, p. 3321 (2009).
[37] O. Gröbner. Beam induced multipacting, Proc. of PAC 1997, Vancouver, Canada, pp 3589-3591 (1997).
[38] F. Zimmermann. Electron-cloud benchmarking and CARE-HHH codes. Proc. of HB2006, Tsukuba, Japan, THBW02 (2006).
[39] W. Bruns, D. Schulte, F. Zimmermann. Factor2: a code to simulated collective effects of electrons and ions. EPAC'06, Edinburgh, Scotland, June 2006, p.2242 (2006).
[40] P. Dijkstal, G. Iadarola, L. Mether, G. Rumolo. Simulation studies on the electron cloud build-up in the elements of the LHC Arcs at 6.5 TeV. CERN-ACC-NOTE-2017-0057, October 2019, Geneva, 2017
[41] L. Wang, A. Chao, H. Fukuma. Short bunch. Presented at ECLOUD'04, Napa, CA, USA.
[42] L. Wang, A. Chao, H. Fukuma. Energy spectrum of an electron cloud with short bunch. Proc. of ECLOUD'04, Napa, CA, USA, CERN-2005-001.
[43] L. Wang, M. Blaskiewicz, H. Hseuh, P. He, Y. Y. Lee *et al*. Multipacting and remedies of electron cloud in long bunch proton machine. Proc. of ECLOUD'04, Napa, CA, USA, CERN-2005-001.
[44] O.B. Malyshev and W. Bruns. ILC DR vacuum design and e-cloud. Proc. of EPAC 2008, Genova, Italy, pp. 673-675 (2008).
[45] R. Cimino, T. Demma. Electron cloud in accelerators. Int. J. Mod. Phys. A **29**, 1430023 (2014).
[46] "Ecloud'12: Joint INFN-CERN-EuCARD-AccNet Workshop on Electron-Cloud Effects, La Biodola, Isola d'Elba, Italy, 5-9 June 2012", ed. by R. Cimino, G. Rumolo, F. Zimmermann, CERN–2013–002, Geneva, 2013.
[47] M.T.F. Pivi, L. Wang, T. Demma, S. Guiducci, Y. Suetsugu, et al. Recommendation for the feasibility of more compact LC damping rings. Proc. of IPAC'10, Kyoto, Japan, 23-28 May 2010, p. 3578 (2010).

[48] Y. Suetsugu, K. Shibata, H. Hisamatsu, M. Shimamoto, M. Shirai and K. Kanazawa. R&D on copper beam ducts with ante-chambers and related vacuum components. Proc. of EPAC'06, Edinburgh, Scotland, June 2006, p. 1438 (2006).
[49] V.V. Anashin, I.R. Collins, O. Gröbner, O.B. Malyshev, N.V. Fedorov, V.P. Nazmov and B.G. Goldenberg. Reflection of photons and azimuthal distribution of photoelectrons in a cylindrical beam pipe. Nucl. Instrum. Methods Phys. Res. A **448**, 76-80 (2000).
[50] V.V. Anashin, I.R. Collins, R.V. Dostovalov, N.V. Fedorov, O. Gröbner, A.A. Krasnov, O.B. Malyshev and E. E. Pyata. Magnetic and electric field effect on the photoelectron emission from prototype LHC bean screen material. Vacuum **60**, 255–260 (2001).
[51] L. Boon and K. Harkay. Chamber surface roughness and electron cloud for the Advanced photon source superconducting undulator. Proc. of ECLOUD12, 5-9 June 2012, La Biodola, Isola d'Elba, p. 95 (2012).
[52] V.V. Anashin, V. Baglin, R. Cimino, I.R. Collins, R.V. Dostovalov, N.V. Fedorov, J. Gómez-Goñi, O. Gröbner, B. Henrist, N. Hileret, A.A. Krasnov, J.-M. Laurent, O.B. Malyshev, E.E. Pyata and M. Pivi. Experimental investigations of the electron cloud key parameters. LHC Project Report 313, October 1999, CERN. - 8 p.
[53] M. Nishiwaki and S. Kato. Graphitization of inner surface of copper beam duct of KEKB positron ring. Vacuum **84**, 743 (2010).
[54] R. Cimino, M. Commisso, D.R. Grosso, T. Demma, V. Baglin *et al*. Nature of the decrease of the secondary electron yield by electron bombardment and its energy dependence. PRL **109**, 064801 (2012).
[55] C. Yin Vallgren, G Arduini, J.Bauche, *et al*. Amorphous carbon coatings for mitigation of electron cloud in the CERN SPS. Proc. of IPAC'10, paper TUPD048 (2010).
[56] M. Nishiwaki and S. Kato. Influence of electron irradiation and heating on secondary electron yields from non-evaporable getter films observed with in situ x-ray photoelectron spectroscopy. J. Vac. Sci. Technol. A **25**, 675 (2007).
[57] L. Calliari, M. Filippi and N. Laidani. Electron beam irradiation of hydrogenated amorphous carbon films. Surf. Interf. Anal. **36**, 1126 (2004).
[58] R. Larciprete, D. R. Grosso, M. Commisso, R. Flammini, R. Cimino. The chemical origin of SEY at technical surfaces. Proc. of ECLOUD12, 5-9 June 2012, La Biodola, Isola d'Elba, p. 99 (2012).
[59] V.V. Anashin, O.B. Malyshev and E.E. Pyata. Photoelectron current from the substrate with cryosorbed gases. Vacuum Technical Note 99-04, April 1999, CERN. -13 p.
[60] V.V. Anashin, A.A. Krasnov, O.B. Malyshev and E.E. Pyata. The effect of the temperature and of a thick layer of condensed CO2 on the photoelectron emission and on the photon reflection. Vacuum Technical Note 99-05, April 1999, CERN. - 10 p.
[61] Y. Suetsugu, K. Kanazawa, K. Shibata and H. Hisamatsu. Continuing study on the photoelectron and secondary electron yield of TiN coating and NEG (Ti-Zr-V) coating under intense photon irradiation at the KEKB positron ring. Nucl. Instrum. Methods Phys. Res. A **556**, p.399 (2006).
[62] P. He, H.C. Hseuh, M. Mapes,R. Todd and D. Weiss. Development of titanium nitride coating for SNS ring vacuum chambers Proc. of PAC'01, p.2159 (2001).
[63] S. Michizono, Y. Saito, Suharyanto, Y. Yamano, S. Kobayashi. Secondary electron emission of sapphire and anti-multipactor coatings at high temperature. Appl. Surf. Sci. **235**, 227-230 (2004).
[64] Suharyanto, S. Michizono, Y. Saito, Y. Yamano, S. Kobayashi. Secondary electron emission of TiN-coated alumina ceramics. Vacuum **81**, 799-802 (2007)
[65] A. Ruiz, E. Román, P. Lozano, M. García, L. Galán, I. Montero, D. Raboso. UHV reactive evaporation growth of titanium nitride thin films, looking for multipactor effect suppression in space applications. Vacuum **81**, 1493-1497 (2007).
[66] W. Fischer, *et al*. Electron cloud observations and cures in Relativistic Heavy Ion Collider. PRST-AB **11**, 041002 (2008).
[67] B. Henrist, N. Hilleret, C. Scheuerlein, M. Taborelli. The secondary electron yield of TiZr and TiZrV non-evaporable getter thin film coatings. Appl. Surf. Sci. **172,** 95-102 (2001).
[68] S. Wang. Secondary electron yield measurements of anti-multipacting surfaces for accelerators. PhD Thesis, Loughborough University, March 2016.
[69] P. Costa Pinto, S. Calatroni, P. Chiggiato, P. Edwards, M. Mensi, H. Neupert, M. Taborelli, C. Yin

Vallgren. Carbon coating of the SPS dipole chambers. Proc. of ECLOUD12, 5-9 June 2012, La Biodola, Isola d'Elba, p. 141 (2012).
[70] N. Bundaleski, S. Candeias, A. Santos, O.M.N.D. Teodoro and A.G. Silva. Study of SEY degradation of amorphous carbon coatings. Proc. of ECLOUD12, 5-9 June 2012, La Biodola, Isola d'Elba, p. 149 (2012).
[71] G.G. Fuentes, R.J. Rodríguez, M.García, L.Galán, I.Montero, J.L.de Segovia. Spectroscopic investigations of Cr, CrN and TiCr anti-multipactor coatings grown by cathodic-arc reactive evaporation App. Surf. Sci. **253**, 7627-7631 (2007).
[72] G. Stupakov and M. Pivi.Suppression of the effective secondary emission yield for a grooved metal surface. Proc of ECLOUD'04, p.139 (2004).
[73] O.B. Malyshev, J.M. Lucas, N. Collomb, S. Postlethwaite, M. Korostelev, A. Wolski, K. Zolotarev. Mechanical and vacuum design of the wiggler section of the ILC damping rings. Proc. of IPAC'10, Kyoto, Japan, 23-28 May 2010, pp. 3563-3565 (2010).
[74] I. Montero, L.Aguilera, M.E. Dávila, V. Nistor, L. Galán, L.A. González, P. Costa Pinto, M.Taborelli and F.Caspers. Novel types of anti-ecloud surfaces. Proc. of ECLOUD12, 5-9 June 2012, La Biodola, Isola d'Elba, p. 153 (2012).
[75] V. Nistor, L.A. González, L. Aguilera, I. Montero, L. Galán, U. Wochner, D. Raboso. Multipactor suppression by micro-structured gold/silver coatings for space applications. Appl. Sur. Sci. **315**, 445-453 (2014).
[76] M. Ye et al., Suppression of Secondary Electron Yield by Micro-Porous Array Structure. J. Appl. Phys. **113**, 074904 (2013).
[77] R. Valizadeh, O.B. Malyshev, S. Wang, S. Zolotovskaya, A. Abdolvand. Low secondary electron yield engineered surface for electron cloud mitigation. App. Phys. Lett. **105**, 231605 (2014).
[78] R. Valizadeh, O. Malyshev. Apparatus and methods relating to reduced photoelectron yield and/or secondary electron yield. Patent publication number WO2015189645 A1. 17th Dec 2015.
[79] R. Valizadeh, O.B. Malyshev, S. Wang, T. Sian, L. Gurran, *et al*. Low secondary electron yield of laser treated surfaces of copper, aluminium and stainless steel. Proc. of IPAC 2016, Busan, Korea, 2016, p.1089.
[80] S. Calatroni, E. Garcia-Tabares Valdivieso, H. Neupert, V. Nistor A. Perez Fontenla, *et al*. First accelerator test of vacuum components with laser-engineered surfaces for electron-cloud mitigation. Phys. Rev. Accel. Beams **20**, 113201 (2017).
[81] R. Valizadeh, O.B. Malyshev, S. Wang, S.A. Zolotovskaya, W.A. Gillespie and A. Abdolvand. Low secondary electron yield engineered surface for electron cloud mitigation. Appl. Phys. Lett. **105**, 231605 (2014).
[82] R. Valizadeh, O.B. Malyshev, S. Wang, T. Sian, M. D. Cropper and N. Sykes. Reduction of Secondary Electron Yield for E-cloud Mitigation by Laser Ablation Surface Engineering. Appl. Surf. Sci. **404,** 370–379 (2017).
[83] Y. Suetsugu, K. Kanazawa, K. Shibata, H. Hisamatsu, K. Oide, F. Takasaki, A.E.Bondar, V. Kuzminykh, A. Gorbovsky, R. Dostovalov, K. Sennyu, H. Hara. R&D of copper beam duct with antechamber scheme for high-current accelerators. Nucl. Instrum. Methods Phys. Res. A **538**, 206-217 (2005).
[84] Y. Suetsugu, K. Shibata, T. Ishibashi, H. Fukuma, M. Tobiyama, J. Flanagan. Achievements and problems in the first commissioning of superKEKB vacuum system. J. Vac. Sci. Technol. A **35**, 03E103 (2017).
[85] K. Zolotarev, O.B. Malyshev, M. Korostelev, A. Wolski, J.M. Lucas, N. Collomb, S. Postlethwaite. SR power distribution along wiggler section of ILC DR. Proc. of IPAC'10, Kyoto, Japan, 23-28 May 2010, pp. 3569-3571 (2010).
[86] Y. Suetsugu, K. Shibata, T. Ishibashi, K. Kanazawa, M. Shirai, S. Terui, and H. Hisamatsu. First commissioning of the SuperKEKB vacuum system. Phys. Rev. Accel. Beams **19**, 121001 (2016).
[87] K. Shibata. SuperKEKB vacuum system. Proc. of ECLOUD12, 5-9 June 2012, La Biodola, Isola d'Elba, p. 67 (2012).
[88] Y. Suetsugu, Y. Tanimoto, Y. Hori, K. Kanazawa, M. Kobayashi and Y-J. Hsu. Effects of external magnetic fields on the photoelectron emission from a copper beam chamber. Proc. of PAC 2001, Chicago, USA, pp. 2180-2182 (2001).

[89] Y. Suetsugu. Observation and simulation of the nonlinear dependence of vacuum pressures on the positron beam current at KEKB. Proc. of PAC 2001, Chicago, USA, pp. 2180-2182.
[90] L. Wang, H. Fukuma, S. Kurokawa, M. Pivi and G. Xia. A perfect electrode to suppress secondary electrons inside the magnets. EPAC'06, Edinburgh, Scotland, June 2006, p. 1489 (2006).
[91] M. Zobov, D. Alesini, A. Drago, A. Gallo, S. Guiducci, C. Milardi, A. Stella, S. De Santis, T.Demma, P. Raimondi. Operating experience with electron cloud clearing electrodes at DAΦNE. Proc. of ECLOUD12, 5-9 June 2012, La Biodola, Isola d'Elba, p. 259 (2012).
[92] D. Alesini, A. Drago, A. Gallo, S. Guiducci, C. Milardi *et al*. Dafne operation with electron-cloud-clearing electrodes. PRL **110**, 124801 (2013).
[93] Y. Suetsugu, H. Fukuma, L. Wang, M. Pivi, A. Morishihe et *al*. Demonstration of electron clearing effect by means of a clearing electrode in a high-intensity positron ring, Nucl. Instr. Meth. Phys. Res. A **598**, 372-378 (2009).
[94] Y. Suetsugu, K. Kanazawa, K. Shibata, T. Ishibashi, H. Hisamatsu, M. Shirai, S. Teru. Design and construction of the SuperKEKB vacuum system. J.Vac.Sci. Technol. A**30** , 031602 (2012).
[95] F. Zimmermann. Electron-cloud simulations for SPS and LHC, CERN-SL-2000-007 DI, Geneva 2000, Proc. of Chamonix X, Chamonix, France, 2000.
[96] H. Bartosik, G. Rumolo. Beams from the injectors. Proc. of 7th Evian workshop on LHC beam operation, Evian Les Bains, France, 2016.
[97] N. Hilleret, V. Baglin, J. Bojko, O. Gröbner, B. Henrist *et al*. The secondary electron yield of technical material and its variation with surface treatments. CERN LHC Project report **433**, Geneva 2000, Proc. of the EPAC'00, Vienna, Austria, 2000.
[98] B. Henrist, N. Hilleret, C. Scheuerlein, M. Taborelli. The secondary electron yield of TiZr and TiZrV non-evaporable getter thin film coating, App. Surf. Sci. **172**, 95-102 (2001).
[99] P. Costa-Pinto, S. Calatroni, H. Neupert, D. Letant-Delrieux, P. Edwards *et al*. Carbon coatings with low secondary electron yield. Vacuum **98**, 29-36 (2013).
[100] P. He, H.C. Hseuh, R. Todd, B. Henrist, N. Hilleret *et al*. Secondary electron emission measurements for TiN coating on the stainless steel of SNS accumulator ring vacuum chamber. Proc. of EPAC'04, Lucerne, Switzerland, 5-9 July 2004, p. 1804.
[101] A.A. Krasnov. Molecular pumping properties of the LHC arc beam pipe and effective secondary electron emission from Cu surface with artificial roughness. Vacuum **73**, 195-199(2004).
[102] V. Baglin, H. Kos. Unpublished, CERN, November 1997.
[103] M. Pivi, F. K. King, R.E. Kirby, T. O. Raubenheimer, G. Stupakov *et al*. Sharp reduction of the secondary electron emission yield from grooved surfaces. J. Appl. Phys. **104**, 104904 (2008).
[104] H. Bruining. Physics and applications of secondary electron emission, Pergamon Press, (1954).
[105] O. Hachenberg *et al.* Secondary electron emission from solids, Adv. Electron Phys. 11413-499 (1959),.
[106] R. Cimino, I.R. Collins. Vacuum chamber surface electronic properties influencing electron cloud phenomena. App. Surf. Sci. **235**, 231-235 (2004).
[107] R. Cimino, L. A. Gonzalez, R. Larciprete, A. Di Gaspere, G. Iadarola *et al.* Detailed investigation of the low energy secondary electron yield of techical Cu and its relevance for the LHC, Phys. Rev. ST Accel. Beams **18**, 051002, (2015).
[108] M.A. Furman. The Electron-Cloud Effect in the Arcs of the LHC. CERN LHC Project Report **180**, 1998 or LBNL-41482/CPB note 247 (1998).
[109] G. Rumolo, F. Ruggiero, F. Zimmermann. Simulation of the electron-cloud build up and its consequences on heat load, beam stability, and diagnostics. Phys. Rev. ST Accel. Beams **4**, 012801 (2001).
[110] R.E. Kirby, F.K. King. Secondary electron emission yields from PEP-II accelerator materials, Nucl. Instr. Meth. Phys. Res. A **469**, 1-12 (2001).
[111] R. Cimino, I. R. Collins, M. A. Furman, M. Pivi, F. Ruggiero *et al*. Can low-energy electrons affect high energy physics accelerators? PRL **93**, 014801 (2004).
[112] I. Maslennikov, W. Turner, V. Anashin, O. Malyshev, V. Osipov, et al. Photodesorption experiments on SSC collider beam tube configurations. Proc. of 1993 IEEE Part. Acc. Conf., Washington, DC, May 17–20, 1993, v. 5, pp. 3876–3878 (1993).

[113] V.V. Anashin, I.R. Collins, R.V. Dostovalov, N.V. Fedorov, et al. Magnetic and electric field effect on the photoelectron emission from prototype LHC bean screen material. Vacuum **60**, 255–260 (2001).
[114] O. B. Malyshev and I.R. Collins. Dynamic Gas Density in the LHC Interaction Regions 1&5 and 2&8 For Optics Version 6.3. LHC-PROJECT-NOTE-**274**, Dec 2001, CERN - 34 pages.
[115] J. Seeman, Y. Cai, J. Clendenin, F-J. Decker, M. Donald *et al*. Status report on PEP-II performance, Proc. of EPAC 2000, Vienna, Austria, pp. 38-42, (2000).
[116] V. Baglin, I.R. Collins, O. Gröbner, C. Grünhagel, B. Henrist *et al*. Measurement at EPA of vacuum and electron cloud related effect. CERN-SL-2001-003, Geneva 2001, Proc. of the LHC Performance Workshop 2001, Chamonix, France.
[117] Y. Suetsugu, K. Kanazawa, K. Shibata, H. Hisamatsu. Recent study on photoelectron and secondary electron yields of TiN and NEG coating using the KEKB positron ring, Nucl. Instr. Meth. Phys. Res. A **578**, 470-479 (2007).
[118] M.T.F. Pivi, G. Collet, F. King, R.E. Kirby, T. Markiewicz et *al*. Experimental observations of in situ secondary electron yield reduction in the PEP-II particle accelerator beam line. Nucl. Instr. Meth. Phys. Res. A **621**, 47-56 (2010).
[119] W.H. Hartung, D. M. Asner, J.V. Conway, C. A. Dennett, S. Greenwald *et al*. In-situ measurements of the secondary electron yield in an accelerator environment: Instrumentation and methods. Nucl. Instr. Meth. Phys. Res. A **783**, 95-109 (2015).
[120] J. M. Jimenez, B. Henrist, N. Hilleret, J-M. Laurent, D. Schulte et *al*. LHC and SPS electron cloud studies. AIP Conference Proceedings **773**, 211 (2005).
[121] R. Larciprete, D. R. Grosso, M. Commisso, R. Flammini and R. Cimino. Secondary electron yield of Cu technical surfaces: Dependence on electron irradiation, Phys. Rev. ST Accel. Beams **16**, 011002 (2013).
[122] R.A. Rosenberg, K. C. Harkay. A rudimentary electron energy analyser for accelerator diagnostics, Nucl. Instr. Meth. Phys. Res. A **453** (2000) 507-513.
[123] G. Arduini, P. Collier, B. Dehning, G. Ferioli, B. Henrist *et al*. Measurements of the electron cloud properties by means of a multi-strip detector in the CERN SPS, Proc. of the EPAC'02, Paris, France, 2002.
[124] K. C. Harkay, R.A. Rosenberg. Properties of the electron cloud in a high-energy positron and electron storage ring, Phys. Rev. ST Accel. Beams **6**, 034402 (2003).
[125] J. Q. Wang, Z. Y. Guo, Y. D. Liu, Q. Qin, J. Xing *et al*. Electron cloud instability studies in the Beijing Electron Positron Collider, Phys. Rev. ST Accel. Beams **7**, 094401 (2004).
[126] U. Iriso, W. Fischer. Electron induced molecular desorption from electron clouds at the Relativistic Heavy Ion Collider, Phys. Rev. ST Accel. Beams **8**, 113201 (2005).
[127] R. J. Macek, A. A. Browman, J. E. Ledford, M. J. Borden, J. F. O'Hara *et al*. Electron cloud generation and trapping in a quadrupole magnet at the Los Alamos proton storage ring, Phys. Rev. ST Accel. Beams **11**, 010101 (2008).
[128] E. Mahner, T. Kroyer, F. Caspers. Electron cloud detection and characterization in the CERN proton synchrotron, Phys. Rev. ST Accel. Beams **11**, 094401 (2008).
[129] M.TF. Pivi, J.S.T. Ng, F. Cooper, D. Kharakh, F. King et *al*. Observation of magnetic resonances in electron clouds in a positron ring, Nucl. Instr. Meth. Phys. Res. A **621**, 33-88 (2010).
[130] K. Kanazawa, H. Fukuma, J. Puneet. Analysis of the electron cloud density measurement with RFA in a positron ring, Proc. of ECLOUD10 workshop, Ithaca, New York, USA, 2010, p. 184.
[131] J.R. Calvey, W.H. Hartung, Y. Li, J.A. Livezey, J. Makita, M. A. Palmer *et al*. Measurements of electron cloud growth and mitigation in dipole, quadrupole, and wiggler magnets, Nucl. Instr. Meth. Phys. Res. A **770**, 141-154 (2015).
[132] J. M. Jimenez, G. Arduini, P. Collier, G. Ferioli, B. Henrist *et al*. Electron cloud with LHC-type beams in the SPS: a review of three years of measurements. Proc. of ECLOUD'02, Geneva, Switzerland, CERN-2002-01 (2002).
[133] J-M. Laurent, U. Iriso Ariz. Particle collectors for electron cloud studies, CERN Vacuum Technical Note 03-05, EDMS: 374712, February 2003, CERN, Geneva, Switzerland.
[134] M. Commisso, T. Demma, S. Giuducci, L. Ping, A. Raco, *et al*. A retarding field detector to measure the actual energy of electrons participating in e-cloud formation in accelerators, Proc. of EPAC'08, Genoa, Italy, 2008, tupc019.

[135] G. Arduini, P. Collier, B. Dehning, G. Ferioli, B. Henrist *et al*. Measurement of the electron cloud properties by means of a multi-strip dectector in the CERN SPS, Proc. of EPAC'02, Paris, France, 2002.
[136] J. M. Jimenez, B. Henrist, N. Hilleret, J-M. Laurent, D. Schulte et *al*. LHC and SPS electron cloud studies. AIP Conference Proceedings 773, 211 (2005).
[137] R. J. Macek, A. A. Browman, M. Borden, D. Fitzgerald, T.S. Wang *et al*. Electron cloud diagnostics in use at the Los Alamos PSR, Proc. of PAC'03, Portland, Oregon, USA, 2003.
[138] B. Henrist, N. Hilleret, J. M. Jimenez, CERN, Geneva, 2002, unpublished.
[139] V. Baglin, B. Jenninger. CERN SPS electron cloud heat load measurements and simulations, Phys. Rev. ST Accel. Beams **6**, 063201 (2003).
[140] O. Brüning, F. Caspers, J-M. Laurent, M. Morvillo, F. Ruggiero. Multpacting tests with magnetic field for the LHC beam screen, Proc. of the EPAC'98, Stockholm, Sweden, 1998.
[141] J-M. Laurent, U. Iriso Ariz. Characterisation of multipacting with a 100 MHz resonant cavity, CERN Vacuum Technical Note 02-12, EDMS: 3488701, June 2002, CERN, Geneva, Switzerland.
[142] K. Welch. Capture pumping technology, North Holland 2001.
[143] V. Baglin. Cold/sticky systems, CERN-2007-003, Proc. of CERN Accelerator School, Vacuum in accelerators, Platja d'Aro, Spain, 2006
[144] V. V. Anashin, O.B. Malyshev, E. E. Pyata. Photoelectron current from the substrate with cryosorbed gases, CERN Vacuum Technical Note 99-04, EDMS: 678255, April 1999, CERN, Geneva, Switzerland.
[145] V. Baglin. The LHC vacuum system: commissioning up to nominal luminosity, Vacuum **138**, 112-119 (2017).
[146] V. Baglin, B. Henrist, N. Hilleret, E. Mercier, C. Scheuerlein. Ingredients for the understanding and the simulation of multipacting, CERN-SL-2000-007 DI, Geneva 2000, Proc. of Chamonix X, Chamonix, France, 2000.
[147] A. Kuzucan, H. Neupert, M. Taborelli, H. Störi. Secondary electron yield on cryogenic surfaces as a function of physisorbed gases, J. Vac. Sci. Technol. A **30**, 051401 (2012).
[148] H. Tratnik. Electron stimulated desorption of condensed gas on cryogenic surfaces, CERN-THESIS-2006-038, PhD Thesis, University Vienna, 2005.
[149] H. Tratnik, H. Hilleret, H. Störi. The desorption of condensed noble gas and gas mixtures from cryogenic surfaces, Vacuum **81**, 731-737 (2007).
[150] V. Baglin, B. Jenninger. Pressure and heat load in a LHC type cryogenic vacuum system subjected to electron cloud, Proc. of ECLOUD'04, Napa, California, USA, CERN-2005-001.
[151] V. Baglin, B. Jenninger. Gas condensates onto a LHC type cryogenic vacuum system subjected to electron cloud, Proc. of EPAC'04, Lucerne, Switzerland, 2004, p. 126.
[152] V. Baglin, Data collected during COLDEX run #93, CERN, July 2003
[153] V. Baglin, I.R. Collins, B. Jenninger. Performance of a cryogenic vacuum system (COLDEX) with a LHC type beam, Vacuum **73**, 201-206 (2004).
[154] LHC design report vol. 1, CERN-2004-003, Geneva, 2004.
[155] O. Gröbner. Vacuum system for LHC. Vacuum 46, 797-801 (1995).
[156] O. Gröbner. Technological problems related to the cold vacuum system of the LHC, Vacuum **47**, 591-595 (1995).
[157] O. Gröbner. Overview of the LHC vacuum system, Vacuum **60**, 25-34 (2001).
[158] J.M. Jimenez. LHC: the world's largest vacuum systems being operated at CERN, Vacuum **84**, 2-7 (2010).
[159] V. Baglin, B. Henrist, J.M. Jimenez, E. Mahner, G. Schneider *et al*. Recovering about 5 km of LHC beam vacuum system after sector 3-4 incident, Proc. of IPAC'10, Kyoto, Japan, 2010, p. 3870.
[160] G. Bregliozzi, V. Baglin, J.M. Jimenez. Summary of beam vacuum activities held during the LHC 2008-2009 shutdown, Proc. of IPAC'10, Kyoto, Japan, 2010, p. 3864.
[161] V. Baglin, G. Bregliozzi, J.M. Jimenez, G. Lanza. Synchrotron radiation in the LHC vacuum system, Proc. of IPAC'11, San Sebastián, Spain, 2011, p 1563.
[162] V. Baglin, G. Bregliozzi, J.M. Jimenez, G. Lanza. Vacuum performances and lessons for 2012, CERN-ATS-2012-069, Geneva 2012, Proc. of Chamonix X, Chamonix, France, 2012, p. 74.

[163] G. Lanza, V. Baglin, G. Bregliozzi, J.M. Jimenez. LHC vacuum system: 2012 review and 2014 outlook, CERN-ATS-2013-045, Geneva 2013, Proc. of 4th Evian workshop on LHC operation, Evian-les-bains, France, 2012, p. 139.
[164] V. Baglin, G. Bregliozzi, P. Chiggiato, J.M. Jimenez, G. Lanza. CERN vacuum system activities during the long shutdown 1: the LHC beam vacuum, Proc. of IPAC'14, Dresden, Germany, 2014, p. 2375.
[165] G. Iadarola, G. Arduini, V. Baglin, H. Bartosik, J. Esteban Muller, G. Rumolo *et al*. Electron cloud and scrubbing studies for the LHC, Proc. of IPAC'13, Shanghai, China, 2013, p. 1331.
[166] V. Baglin. How to deal with leaks in the LHC beam vacuum, CERN-AB-2005-014, Geneva 2005, Proc. of Chamonix 2012 LHC performance workshop, Chamonix, France, 2005, p. 105.
[167] V. Baglin. Vacuum transients during LHC operation, CERN-AB-2004-014 ADM, Geneva 2004, Proc. of Chamonix XIII, Chamonix, France, 2004, p. 275.
[168] J.M. Jimenez, S. Antipov, G. Arduini, A. Bertarelli, N. Biancacci, B. Bradu *et al*. Observations, analysis and mitigation of recurrent LHC beam dumps caused by fast losses in arc half-cell 16L2. Proc. IPAC2018, Vancouver, Canada, April-29 to May, 4, 2018, p. 228 (2018).
[169] Data of the National Institute of Standards and Technology from atomic and molecular databases. Electron-impact cross sections for ionisation and excitation database. https://www.nist.gov/pml/electron-impact-cross-sections-ionization-and-excitation-database
[170] W. Fischer, M. Blaskiewicz, J.M. Brennan, H. Huang, H-C. Hseuh *et al*. Electron cloud observations and cures in the Relativistic Heavy Ion Collider. Phys. Rev. ST Accel. Beams **11**, 041002 (2008).